

Alma Mater Studiorum Università di Bologna
Archivio istituzionale della ricerca

Continuous Liquid-Phase Upgrading of Dihydroxyacetone to Lactic Acid over Metal Phosphate Catalysts

This is the final peer-reviewed author's accepted manuscript (postprint) of the following publication:

Published Version:

Giada Innocenti, E.P. (2020). Continuous Liquid-Phase Upgrading of Dihydroxyacetone to Lactic Acid over Metal Phosphate Catalysts. ACS CATALYSIS, 10, 11936-11950 [10.1021/acscatal.0c03761].

Availability:

This version is available at: <https://hdl.handle.net/11585/779407> since: 2020-11-10

Published:

DOI: <http://doi.org/10.1021/acscatal.0c03761>

Terms of use:

Some rights reserved. The terms and conditions for the reuse of this version of the manuscript are specified in the publishing policy. For all terms of use and more information see the publisher's website.

This item was downloaded from IRIS Università di Bologna (<https://cris.unibo.it/>).
When citing, please refer to the published version.

(Article begins on next page)

This is the final peer-reviewed accepted manuscript of:

G. Innocenti, E. Papadopoulos, G. Fornasari, F. Cavani, A. J. Medford, C. Sievers

Continuous liquid-phase upgrading of dihydroxyacetone to lactic acid over metal phosphate catalysts

ACS Catalysis 10 (2020) 11936

The final published version is available online at:
<https://dx.doi.org/10.1021/acscatal.0c03761>

Terms of use:

Some rights reserved. The terms and conditions for the reuse of this version of the manuscript are specified in the publishing policy. For all terms of use and more information see the publisher's website.

This item was downloaded from IRIS Università di Bologna (<https://cris.unibo.it/>)

When citing, please refer to the published version.

Continuous liquid-phase upgrading of dihydroxyacetone to lactic acid over metal phosphate catalysts

Giada Innocenti,^{a,b,c} Eleni Papadopoulos,^a Giuseppe Fornasari,^b Fabrizio Cavani,^{b,c} Andrew J. Medford,^a and Carsten Sievers^{a,*}

^a School of Chemical & Biomolecular Engineering, Georgia Institute of Technology, 311 Ferst Dr. NW Atlanta, GA, 30332, United States

^b Dipartimento di Chimica Industriale "Toso-Montanari", Università di Bologna, Viale del Risorgimento 4, Bologna, 40136, Italy

^c Consorzio INSTM, Research Unit of Bologna, Firenze, Italy

* Corresponding author: carsten.sievers@chbe.gatech.edu

Abstract

The performance of Brønsted and Lewis-acidic La, Nb, and Zr phosphates (LaPO, NbPO and ZrPO) during aqueous phase conversion of dihydroxyacetone (DHA) to lactic acid (LA) is investigated using a fixed-bed reactor. Mass transfer phenomena are thoroughly investigated, and the mass transfer coefficient is deconvoluted from the intrinsic kinetic constant for each catalyst. NbPO is found to be mass transfer limited. Despite this limitation, NbPO shows the highest yield of lactic acid at 36 %. The reaction over ZrPO is not transport limited, and the conversion of DHA into pyruvaldehyde (PVA) is following a second-order reaction mechanism. Additionally, a correlation between lactic acid production and the carbon missing from the carbon balance (carbon loss) is observed. Finally, NbPO and ZrPO show stable performance up to 10 h on stream during deactivation tests. After 15 h of reaction, the pyruvaldehyde yield increases at the expense of lactic acid with NbPO. This is ascribed to a deactivation of the active sites necessary to produce lactic acid, which are different from the sites that produce pyruvaldehyde. This hypothesis is supported by the characterization of the spent catalyst with ¹³C magic-angle spin nuclear magnetic resonance and attenuated total reflectance infrared spectroscopy.

Keywords: Mass-transfer, kinetic, second order reaction, plug flow reactor, deactivation, pyruvaldehyde, acid catalysts

Introduction

In the last decades, concerns regarding oil depletion and environmental issues have driven developments in biofuel production and research.^{1–3} In particular, biodiesel production by triglyceride transesterification with methanol to fatty acid methyl esters (FAME) exponentially increased in recent years.⁴ Since biodiesel production yields 10 wt% of glycerol as a by-product, there is a significant excess of the latter on the world market. The combination of glycerol supply and the limited profit margins for biofuels have motivated significant research of glycerol valorization that could help make biodiesel production economically sustainable.^{5,6}

The conversion of glycerol into lactic acid (LA) is one of the most studied possible upgrading strategies.⁷ LA is interesting because it can be used to produce the biopolymer poly(lactic acid)

(PLA), which is widely used by the medical industry and, thanks to its biodegradability, the packaging industry.^{8–11} In 2013, the global demand for LA was estimated to be 714 kilotons and is expected to reach 1960 kilotons by 2020, with global market size of 9.8 billion USD by 2025.^{12,13}

Lactic acid can be produced from glycerol through either a one-pot selective oxidation using supported metal catalysts or a two-step reaction.^{7,14} In the second approach, glycerol is first converted into dihydroxyacetone (DHA) by aerobic catalytic oxidation and then further converted into LA (Figure 1).¹⁵ The second processing step of this two-step scheme is an area of continuing investigation and the focus of this contribution.^{16–20}

A study published in 1992 on the prebiotic synthesis of hexose sugars from glyceraldehyde using Fe(OH)O reports lactic acid as a side product.²¹ However, the attention towards the conversion of trioses into lactic acid grew after the study published in 2005 by Hayashi et al.²² Recently, Jolimaitre et al.²³ proposed a kinetic model that well describe homogeneous catalysts behavior and were able to distinguish the contribution of different ionic species in the evolution of the kinetic parameters for Al(SO₄)₃.

The catalytic performances of Brønsted acids, such as H₂SO₄^{18,23,24}, HCl^{18,24}, and H₃PO₄^{18,25}, were also studied. For those catalytic systems, the main product was pyruvaldehyde (PVA) with only trace amounts of LA. These results show that Brønsted acid sites can efficiently produce PVA, but are not involved in lactic acid formation. The main drawbacks of homogeneous catalysis are separation and corrosion issues, making a heterogeneous process highly desirable. The reaction mechanism hypothesized for homogeneous catalysis, reported in Figure 1, is equally valid for heterogeneous catalysts. In fact, it is generally accepted that glyceraldehyde (GLA) can isomerize on Lewis acid sites to DHA, which is the more stable isomer.^{23,26} Furthermore, Rasrendra et al.²⁴ found that if DHA is used as substrate PVA and LA are observed as products, while the GLA concentration is very low. On the contrary, when GLA is used as the substrate, its concentration rapidly drops in favor of DHA and PVA, and only at longer reaction times, the LA concentration starts to be significant. Triose dehydration can be catalyzed by mild Brønsted acids.²⁷ The dehydration can be assisted even by Lewis acid sites, but it occurs more efficiently in the presence of Brønsted acidity.^{23,28,29} Finally, PVA is converted into LA or alkyl lactate over Lewis acid sites *via* the Cannizzaro reaction, and the presence of strong Brønsted acid sites leads to PVA diacetal formation as a side product in alcoholic solvents.³⁰

According to the active site requirements, the ideal heterogeneous catalyst possesses Brønsted and Lewis acid sites with a specific strength.

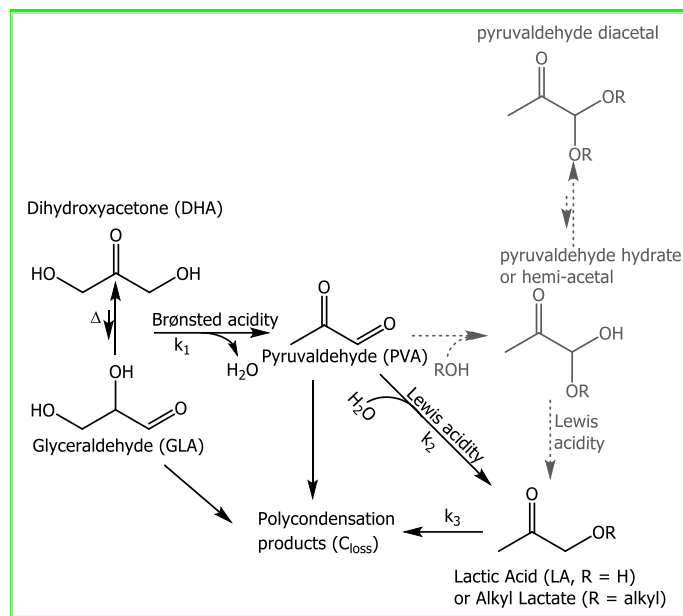


Figure 1. DHA upgrading mechanism into LA or alkyl lactate in aqueous ($R=H$, black) or alcoholic ($R=alkyl$, gray) solvent, respectively. The formation of polycondensation products is modeled in this work as k_3 while the DHA dehydration and the Cannizzaro reaction of PVA as k_1 and k_2 , respectively.

Commercial zeolites³¹, desilicated zeolites,³² Ga-zeolites,^{16,33} Sn-zeolites^{17,34–36}, Nb-zeolites,³⁷ Ru-zeolites,³⁸ Cr-Ti/SiO₂,³⁹ Pt(dppe) supported on montmorillonite,⁴⁰ ZrO₂ based mixed oxide⁴¹, deformed orthorhombic phase Nb₂O₅,²⁰ Sn-Al₂O₃,⁴² Sn-Nb₂O₅,⁴³ Sn-silica mesoporous material (MCM-41)^{44,45}, Sn-Porous Carbon Silica Material (CSM)¹⁹, Sn-hydroxyapatite⁴⁶, Sn-montmorillonite⁴⁷, and modified Sn-phosphates^{25,48} were proposed as catalysts. Unfortunately, zeolites and similar materials suffer from limited hydrothermal stability. For example, when USY is exposed to LA in an aqueous environment at elevated temperature its framework is irreversibly damaged leading to loss of pore volume, surface area, and acidity.²⁸ However, when MeOH is used as a solvent only minor damage was observed. A majority of the studies reported in literature use alcoholic solvents producing alkyl lactates, which need to be hydrolyzed to lactic acid to produce PLA requiring additional conversion and separation steps.^{19,37} Easy and cheap synthesis procedures were proposed for SnP-PEG2000²⁵ and siliceous-tin phosphate catalysts⁴⁸, since the synthesis of porous materials is often expensive and not easily scalable.⁴⁹ The main drawbacks of tin-containing catalysts for industrial applications are its scarcity and, typically, complex and lengthy synthesis procedures.^{16,32,33} Recently, Wang et al.⁵⁰ attempted to address the problem of lengthy synthesis procedures by proposing a SnO₂ – doped NbOPO₄ - CTAB synthesized by sol-gel. SnPO, along with ZrPO, is also the object of a Chinese patent application for C3 and C6 sugar conversion into lactic acid.⁵¹ Metal phosphates are interesting for dihydroxyacetone upgrading in water, thanks to their well-known water tolerance.⁵² Furthermore, the use of ZrPO, NbPO, and SnPO is well documented in carrying out reactions requiring both Brønsted and Lewis acid sites, such as HMF production from sugars.^{53–55} Reproducible performance (a small decrease in conversion at constant yield) was shown for phosphates used in sugar conversion for up to 5 reuses. However, all the studies mentioned so far were done using a batch reactor, which is less appealing for scale-up and industrial production than a flow reactor.⁵⁶ A flow reactor allows continuous production, an evident economic advantage, since it requires less scheduled downtime and can facilitate product transportation.^{57,58} Even on a lab-scale, the flow reactors are more efficient for studying reaction kinetics, transport phenomena, and catalyst deactivation.⁵⁹ The increased use of continuous flow processes in academic laboratories is critical to assess catalytic reactions for biomass valorization in a way that can be extrapolated towards scale-up.

To our knowledge, only two studies dealt with DHA transformation into alkyl lactate or lactic acid using a continuous flow set up. Mylin et al.⁴¹ studied the activity of amphoteric ZrO₂-based mixed oxides, both in batch and continuous flow setups, using ethanol as solvent. ZrO₂-TiO₂ in a continuous flow system yielded 90% ethyl lactate at 140 °C. DHA conversion was stable for 7 h, while the ethyl lactate yield decreased by 15% over that time. A comparison between the autoclave and the continuous flow results showed that the reaction under flow conditions allows for higher LA yields, but no explanation was provided for this performance enhancement. West et al.⁶⁰ studied the catalytic performance of H-USY-6 (FAU) zeolite in a batch and continuous liquid phase set-up. In the continuous liquid phase tests at 177 °C, H-USY-6 showed continuous deactivation when H₂O was used as the solvent, while its stability in this set-up increased using MeOH. The deactivation was attributed to both carbon deposition and framework degradation. A catalyst able to work in water without strongly deactivating is highly desirable since water is the greenest and cheapest solvent and also allows for the direct production of lactic acid.⁵² A cheap, easily synthesizable, and water-tolerant catalytic system needs to be developed. La, Zr, and Nb phosphates are reported among the water-tolerant solid acid catalysts,⁵² but their catalytic activity for DHA conversion to LA, especially in a continuous liquid flow reactor, still needs to be assessed.

In this contribution, we investigate Nb, Zr, and La phosphates for LA production from DHA using water as the solvent **in a Plug Flow Reactor**. The materials are fully characterized in terms of specific surface area, porosity, and acidity. Their performances in a continuous liquid phase setup as a function of temperature, contact time, and time on stream are evaluated. The roles of mass transfer and intrinsic kinetics for these catalysts are thoroughly analyzed. Finally, the spent catalysts are characterized to obtain insight into the reasons for their deactivation.

Methods

Catalyst syntheses

Three different metal phosphate catalysts (ZrPO, LaPO, NbPO) were synthesized by coprecipitation using methods adapted from the literature.^{61–64}

LaPO was synthesized by slowly adding an aqueous 0.8 M La(NO₃)₃ 6H₂O solution (130 mL) to a continuously stirred 1.2 M H₃PO₄ solution (130 mL). Then, the pH was adjusted to 7 using NH₄OH, and the precipitate was aged under ambient conditions for 2 h. This was then filtered, washed, and dried at 80 °C overnight.⁶¹

ZrPO synthesis followed a similar procedure. Specifically, an aqueous 1 M ZrOCl₂ 8H₂O solution (64 mL) was added dropwise to a 1 M NH₄H₂PO₄ solution (128 mL). In this case, the pH was not adjusted before aging the precipitate; which was then filtered, washed, and dried at 80 °C overnight.^{63,64}

NbPO was synthesized using hexadecyl amine as the templating agent to enhance its surface area. Following a typical procedure, 100 mL of a 0.4 M H₃PO₄ ethanol solution was added dropwise to 100 mL of a 0.2 M NbCl₅ ethanol solution. The obtained solution was vigorously stirred for 30 min. Afterward, the pH was adjusted to 2.6 with NH₄OH to obtain a white precipitate. The precipitate was filtered, washed, and added to a 0.6 M hexadecyl amine solution. The new slurry was aged for 30 min while stirring, then the pH was adjusted to 3.5 with 85 % w/w H₃PO₄. The obtained gel was aged in a Teflon autoclave for 2 days at 65 °C. Finally, the precipitate was filtered, washed, and dried in an oven overnight.⁶²

LaPO, ZrPO, and NbPO, after drying, were calcined at 550 °C,⁶⁴ 400 °C,⁶³ and 800 °C, respectively.

The calcination temperature for NbPO is the minimum necessary to completely remove the templating agent. In a temperature screening, 800 °C proved to be the minimum temperature at which the catalyst was free of coke residues after burning the templating agent.

Catalyst characterization

X-ray diffraction (XRD) patterns were recorded in the range of $10^\circ < 2\theta < 80^\circ$ with a Philips PW 1050/81 apparatus controlled by a PW1710 unit ($\lambda = 0.15418$ nm (Cu), 40 kV, 40 mA). The scanning rate was $0.05^\circ 2\theta \text{ s}^{-1}$ and the step time 1 s. Crystalline phases were identified using the "Search and match!" option of X'Pert Highscore Plus and the ICSD database.

Nitrogen physisorption measurements were performed at -196°C using a Micromeritics ASAP 2020 physisorption analyzer. The catalysts were degassed at 200°C for 4 h before measurement. Surface areas and mesopore volumes were calculated based on the BET method⁶⁵ and BJH method,⁶⁶ respectively.

Attenuated total reflectance (ATR) IR spectra of the fresh materials, without any pre-treatment, were recorded at room temperature with an ALPHA-FTIR instrument at a resolution of 2 cm^{-1} after 64 scans. The spectrometer was equipped with a DLaTGS and a single reflection diamond. The ATR spectra of the catalyst after reaction were performed on a Thermo Fisher Scientific Nicolet iS10 instrument with a Smart iTR ATR sampling accessory at a resolution of 4 cm^{-1} after 64 scans. The instrument was equipped with an MCT/A detector, and the accessory had a single reflection ZnSe crystal.

^{31}P and ^{13}C MAS NMR spectra were measured with a Bruker Avance III HD 300 solids spectrometer. A rotor with an outer diameter of 4 mm and 16 mm length was loaded with the sample. The spinning rate was 10 kHz, and the chemical shifts were referenced at 0 ppm with respect to ammonium-dihydrogen-phosphate and adamantane for ^{31}P and ^{13}C , respectively. ^{31}P MAS NMR spectra were acquired using a recycle delay of 5 s. The pulse length was $1 \mu\text{s}$, and the spectra were acquired with 256 scans with a dwell time of $2 \mu\text{s}$. ^{13}C -MAS NMR spectra were measured with cross-polarization to characterize the carbonaceous residues on the catalyst surface after the reaction. The spectrum was acquired as the sum of 4096 scans with a dwell time of $22 \mu\text{s}$ and a recycle time of 10 s.

The amount of carbon deposition on the catalyst surface after the reaction was evaluated using an SDT-Q600 thermogravimetric analyzer (TGA) by TA Instruments. The sample after the reaction was left to dry at room temperature and pressure for 3 days. The dried sample was initially stabilized at 25°C for 10 min in N_2 flow (50 ml min^{-1}). Afterward, the carrier was switched to air (50 ml min^{-1}) and the temperature was raised at $10^\circ\text{C min}^{-1}$ to 800°C . The sample remained at the highest temperature for 10 min.

Total acid site strength and concentration of the catalyst were determined by NH_3 temperature-programmed desorption (NH_3 -TPD) using a Micromeritics Autochem II 2920. A 50 mg powder sample was placed in a U-shaped fixed-bed reactor, preheated at 400°C for 1 h, and cooled to 100°C . Then, gaseous NH_3 was injected to saturate the sample, followed by the introduction of He as a carrier gas to purge the excess of NH_3 . After stabilization for 1 h, the sample was heated to 700°C at a ramping rate of $10^\circ\text{C min}^{-1}$. NH_3 desorption profile in the temperature range of $100 - 700^\circ\text{C}$ was measured using a thermal conductivity detector (TCD).

The Brønsted and Lewis acidity was evaluated by pyridine adsorption followed by Fourier Transform Infrared (FTIR) Spectroscopy. The experiments were performed using a Thermo Fisher Scientific Nicolet iS10 instrument with an MCT/A detector. Each sample was loaded into a vacuum transmission cell as a self-supported wafer (diameter 1.25 cm). The sample was activated at 450°C for 1 h under

high vacuum. A background spectrum was recorded at 150 °C. Then, pyridine (0.1 mbar) was dosed for 30 minutes. Subsequently, the cell was evacuated for 1 h to remove the physisorbed pyridine. Temperature-programmed desorption was carried out to determine the strength of acid sites. The sample was heated to 250 °C, 350 °C, and 450 °C for 1 h, but each 'high temperature' spectrum was taken at 150 °C. The concentration of Lewis and Brønsted acid sites was determined using the Lambert-Beer equation

$$C_w = \frac{A_{peak} \cdot S}{W \cdot \varepsilon} \quad (1)$$

where C_w ($\mu\text{mol g}^{-1}$), W (g), S (cm^2), and ε ($\text{cm}^2 \mu\text{mol}^{-1}$) indicate weight-based site concentration, sample weight, sample disk area, and the integrated molar extinction coefficient, as reported by Tamura et al., respectively.⁶⁷ By integrating the peaks around 1445 cm^{-1} and 1545 cm^{-1} after exposure to each temperature, the concentrations and strength of Lewis and Brønsted acid sites, respectively, were evaluated. The higher the temperature of pyridine desorption, the stronger its interaction with the acid site.

The concentrations of elements from Na to U present in the samples were detected by Proton Induced X-ray Emission (PIXE) analysis, performed by Elemental Analysis Inc.⁶⁸

X-Ray fluorescence analysis (XRF) was used to evaluate the catalyst leaching during a batch reaction at 90 °C using a Parr reactor. A PANalytical Axios Advanced dispersive wavelength spectrometer, equipped with a 4kW power rhodium tube, was used for analysis.

Catalytic reactions

Catalytic conversion of dihydroxyacetone was studied in an up-flow fixed bed reactor (1/4 in Swagelok 316 stainless steel tube). Quartz wool was used in both ends of the reactor to keep the catalyst bed in place. The reactor temperature was varied between 90 °C and 150 °C, and the pressure was set at 10 bar using an Equilibar EB1LF2 back pressure regulator with a PTFE/glass diaphragm. A 0.4 M dihydroxyacetone aqueous solution was pumped by an Agilent 1100 Series HPLC pump at a flow rate of 0.2 mL min^{-1} (except where otherwise noted). In a typical experiment, 200 mg of catalyst (90 – 212 μm) were loaded, and the reaction products were collected every 30 min for 6 h with the aid of an automatic Valco selector valve. All the collected samples were filtered using a 0.45 μm polypropylene membrane before analysis. The system requires about 1.5 h to reach a steady state.

All aliquots were analyzed by high-performance liquid chromatography (HPLC) in an Agilent 1260 Infinity HPLC equipped with a refractive index detector (RID). A Rezex ROA-H⁺ column was used at 60 °C in isocratic elution mode with a 0.0025 mol L^{-1} H_2SO_4 solution as a mobile phase at a flow rate of 0.6 mL min^{-1} . The RID temperature was kept at 50 °C.

The flow rate was varied (0.1 - 0.3 mL min^{-1}), and the amount of catalyst in the reactor was adjusted to maintain constant space-time to determine any external mass transfer limitations. To evaluate potential pore diffusion limitations, the catalyst particle size was varied from 38 – 75 μm to 355 – 425 μm .

Since the apparent density varies among the three catalysts (0.82, 0.57, 0.38 g mL^{-1} for LaPO, ZrPO, and NbPO, respectively), the space-time is expressed as follows:

$$W/F = \frac{m}{\dot{V}_{tot}} \quad (2)$$

$$\tau = \frac{W/F}{\rho_a} \quad (3)$$

where m (in g) is the loaded catalyst mass in the reactor, \dot{V}_{tot} is the total volumetric flow in mL s^{-1} , and ρ_a is the apparent density in g mL^{-1} . When the space time is expressed as mass to total volumetric flow (W/F) ratio the units are g s mL^{-1} . The contact time (τ) is obtained by dividing the W/F by the apparent density of the catalyst and it is expressed in s. These two numbers represent how long the catalyst is contacted with the reactant with respect to the mass (W/F) or the Volume (W/ρ_a) of catalyst in the reactor. In the deactivation section, the data are reported with respect to the time on stream (in h) which, at the steady state for a PFR reactor, represent how long the reaction was carried out and in absence of deactivation it does not affect the activity of the catalyst.

Dihydroxyacetone conversion (X_{DHA}), product selectivities (S_p), and yields (Y_p) were determined using the following equations:

$$X_{DHA} = \frac{C_{DHA}^{in} - C_{DHA}^{out}}{C_{DHA}^{in}} \cdot 100 \% \quad (4)$$

$$Y_p = \frac{C_p^{out} \cdot z_p}{C_{DHA}^{in} \cdot z_{DHA}} \cdot 100 \% \quad (5)$$

$$S_p = \frac{Y_p}{X_{DHA}} \cdot 100 \% \quad (6)$$

where C_{DHA}^{in} is the initial number of moles of DHA, C_{DHA}^{out} is the final number of moles of DHA, C_p^{out} is the number of moles of the product of interest, while z_p and z_{DHA} are the carbon atom number of the product of interest and DHA, respectively. The amount of carbon lost to the formation of deposits or undetected products was evaluated as the difference between the conversion and the sum of the yields of detected products. For this reason, when the carbon loss was slightly negative, it was forced to zero, and the yield sum was assumed to equal the conversion. This mathematical imposition was necessary only at low temperatures (90°C).

A detailed methodology for the kinetic analysis, the evaluation of the activation energy and the mass transfer is reported in the Supplementary Information.

Results and discussion

Catalyst structure and compositions

The catalyst surface properties such as pore size, pore-volume, and surface area were evaluated by N_2 -physisorption. All the catalysts showed a type IV hysteresis curve characteristic of mesoporous materials, as shown in Figure S1. LaPO presented the lowest surface area and the largest mesopore width (Table 1). On the contrary, ZrPO possessed the highest surface area and the mesopore

distribution shifted towards the micropore region, while NbPO showed the lowest cumulative pore volume and the smallest average mesopore width.

The composition of the catalysts was analyzed by PIXE analysis to detect all contaminants present (Table S1) and to evaluate the metal-phosphorous (M/P) ratio (Table 1).

XRD showed that NbPO and ZrPO were almost completely amorphous, while LaPO was semi-crystalline (Figure 2A). According to the XRD patterns, the dominant crystalline phase in LaPO was LaPO_4 (Ref. 00-032-0493), as expected. This result generally agrees with the La/P ratio (0.80) of the sample. The intense diffraction at 20.56° in the X-ray diffractogram of NbPO could be assigned to the most intense diffraction of $\text{Nb}_{1.91}\text{P}_{2.82}\text{O}_{12}$ (Ref. 00-051-1738) or NbPO_5 (Ref. 00-019-0868). Since the Nb/P ratio of 0.62 is in excellent agreement with the theoretical Nb/P ratio (0.67) of the $\text{Nb}_{1.91}\text{P}_{2.82}\text{O}_{12}$ phase, the second possibility was rejected. The broad diffraction around 20° in the X-ray diffractogram of ZrPO was in agreement with the most intense diffraction of either $\text{Zr}_2\text{O}(\text{PO}_4)_2$ (Ref. 00-037-0155) or $\text{Zr}(\text{HPO}_4)_2 \cdot n\text{H}_2\text{O}$ (Ref. 00-019-1489). The Zr/P ratio of 0.31 obtained by PIXE analysis was in better agreement with the $\text{Zr}(\text{HPO}_4)_2 \cdot n\text{H}_2\text{O}$ phase than with $\text{Zr}_2\text{O}(\text{PO}_4)_2$. The disagreement between the PIXE M/P ratio and the phase found with XRD suggested that probably all these samples were a mixture of phases.

Table 1. BET surface area (S_{BET}), BJH desorption cumulative pore volume (BJH_{DPV}), BJH desorption average pore width (BJH_{DPW}), and the total concentration of acid sites determined by NH_3 -TPD.

Entry	Catalyst	M/P ratio	S_{BET} $\text{m}^2 \text{g}^{-1}$	BJH_{DPV} $\text{cm}^3 \text{g}^{-1}$	BJH_{DPW} nm	NH_3 -TPD $\mu\text{mol m}^{-2}$	$\mu\text{mol g}^{-1}$
1	ZrPO	0.31	122	0.175	9.48	5.20	634
2	NbPO	0.62	69	0.144	7.97	4.07	281
3	LaPO	0.80	56	0.177	14.07	4.80	269

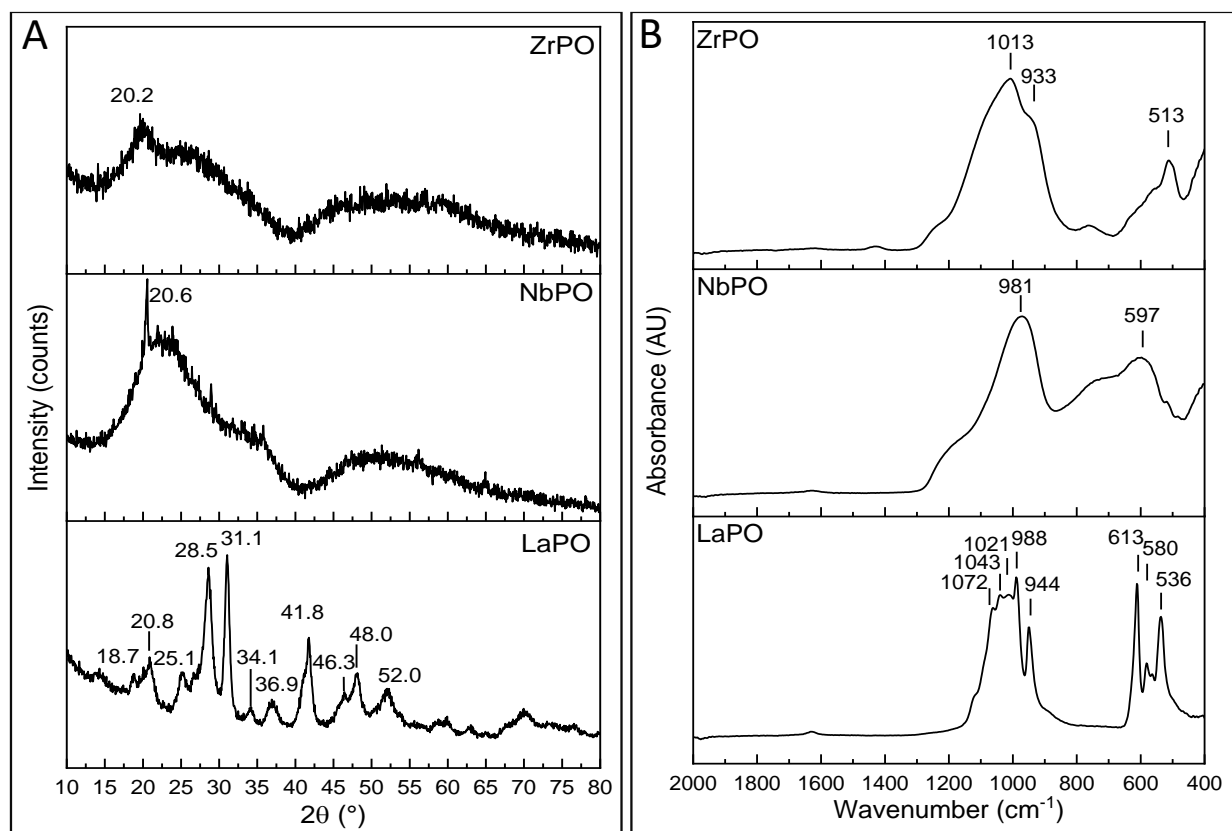


Figure 2. A: XRD patterns for LaPO, ZrPO, and NbPO; B: LaPO, ZrPO, NbPO surface ATR-IR spectra.

Since two of the three catalysts were predominantly amorphous, they were also studied by ATR-FTIR spectroscopy to obtain some information about their P-O bonds (Figure 2B). Broad phosphates bands (around 1000 cm^{-1} , P-O asymmetrical stretching vibration, and $500\text{--}600\text{ cm}^{-1}$, PO_4 deformation modes) verified the amorphous character of NbPO and ZrPO. Additionally, the multiple high and sharp lines present in LaPO ATR spectrum confirmed its semi-crystallinity.⁶¹ In fact, the strong crystal field of LaPO splits the asymmetrical P-O stretching (ν_3) into four bands detectable at 1072 cm^{-1} , 1043 cm^{-1} , 1021 cm^{-1} , and 988 cm^{-1} ; and the deformation vibration (ν_4) into three peaks at 613 cm^{-1} , 580 cm^{-1} , and 536 cm^{-1} , respectively.^{69–72} Thanks to the high LaPO crystal field, even the symmetrical stretching vibration (ν_1) at 944 cm^{-1} was resolved although it should be infrared forbidden.⁷¹ The broad-band around 750 cm^{-1} in the spectra of NbPO and ZrPO is attributed to the P-O-P vibration of diphosphate groups.⁷³ The ZrPO band at 933 cm^{-1} was already observed in the α -zirconium hydrogen phosphate FTIR spectrum.⁷³ The peak position of asymmetric P-O stretching vibrations usually increases in energy with increasing ionic radius of the cation, which is in agreement with our experimental results (Nb (215 pm) < Zr (230 pm) < La (250 pm) \rightarrow 981 cm^{-1} < 1013 cm^{-1} < 1072 cm^{-1} , respectively). The increase in P-O vibration frequency means that the ionic character of the M- PO_4 bond is increasing as the number of PO_4^{3-} moieties in the crystal cell is decreasing.

^{31}P MAS NMR spectroscopy was used to gain further information regarding phosphate species in the entire samples, including amorphous domains (Figure 3). For crystalline materials, the number of peaks in ^{31}P MAS NMR spectra for orthophosphates is equivalent to the number of non-equivalent P atoms in the catalyst structure.⁷⁴ The nomenclature for phosphate connectivity in solids depends on the number of PO_4 bridging oxygen, n . In the phosphate case, there are five possibilities from Q^0 (no M-O-P bond is present) to Q^4 (all the oxygen atoms are involved in M-O-P bonds).⁷⁵ It was possible to deconvolute the spectra of ZrPO, NbPO, and LaPO using 4, 2, and 1 Gaussian curves (Figure S2). The resonance at 4.0 ppm in the spectrum of LaPO was attributed to tetrahedral PO_4 connected to two La atoms (Q^2 topology).⁷⁴ This assignment is consistent with the monoclinic $\text{P2}_1/n$ space group characteristic for the LaPO_4 phase. The chemical shifts for the resonances of NbPO were 9.3 and 24.6 ppm . The peak at 24.6 ppm can be assigned to a Q^4 topology since it is assumed that the octahedral NbO_6 and the tetrahedral PO_4 share all the vertices. Therefore, every oxygen atom is linked to an Nb and a P atom in the $\text{Nb}_{1.61}\text{P}_{2.8}\text{O}_{12}$ phase.⁷⁶ The resonance at 9.3 ppm can be attributed to defects that decrease the number of bridging oxygen atoms.⁷⁷ The ^{31}P MAS NMR spectrum of ZrPO contained four signals at 26.7 , 21.0 , 12.4 , and 5.4 ppm . In this case, it was possible to attribute the signals at 26.7 ppm , 21.0 ppm , and 12.4 ppm to Q^4 , Q^3 , and Q^2 topology of zirconium hydrogen phosphate (HPO_4).⁷⁵ The peak at 9.3 ppm in the spectrum of NbPO and that at 5.4 ppm in the spectrum of ZrPO, are tentatively assigned to a Q^2 topology of PO_4 . This assignment is in good agreement with the correlation between the electronegativity of the metal center and the isotropic chemical shift. In fact, by decreasing the metal electronegativity, P attracts more electron density and strengthens the P-O bond, causing an upfield shift of the chemical shift.⁷⁵ The electronegativity of Nb, Zr, and La is 1.6 , 1.3 , and 1.1 , respectively. Moreover, in light of this result and the presence of the shoulder at 933 cm^{-1} in ATR-IR spectrum, it is possible to hypothesize that the main phase of ZrPO is α -zirconium phosphate ($\text{Zr}(\text{HPO}_4)_2 \cdot n\text{H}_2\text{O}$), which has a Zr/P ratio closer to the one obtained from the PIXE analysis (0.31). However, it is not possible to completely exclude the presence of $\text{Zr}_2\text{O}(\text{PO}_4)_2$ or some other phosphate (or hydrogen phosphate) phase due to the amorphous character of this sample.

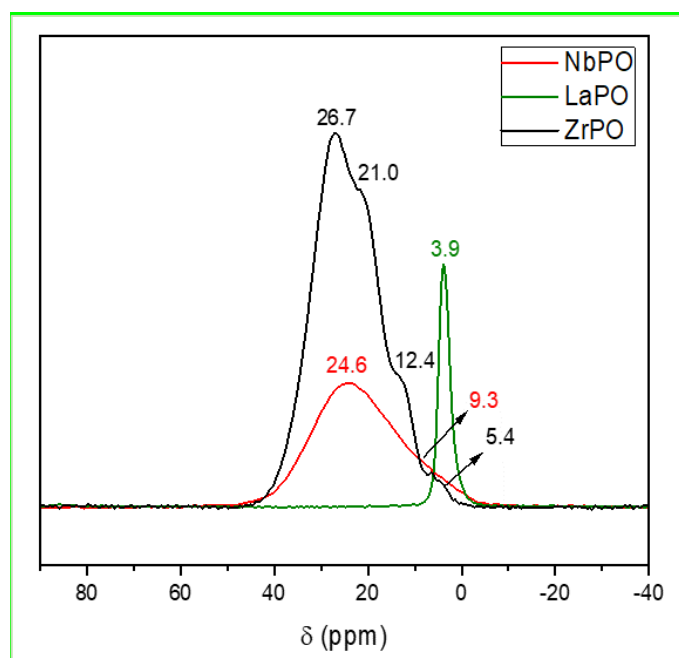


Figure 3. ^{31}P -MAS NMR spectra of NbPO, LaPO, and ZrPO.

Concentration and strength of acid sites

The acid site concentration on the catalysts was evaluated by NH_3 -TPD. ZrPO possessed the highest acid site density (Table 1) and showed a very broad desorption peak from 100 °C to 450 °C (Figure S3A). It presented an absolute maximum around 180 °C and a defined shoulder centered around 290 °C. On the contrary, NbPO showed the lowest total acidity and a broad desorption profile (from 100 °C to 400 °C). In this case, the peak maximum is at 190 °C. The desorption curve for LaPO had a maximum centered around 160 °C. The catalysts can be placed in order, based on the density of acid sites, as follows: ZrPO > LaPO > NbPO.

Since the reaction is known to be driven by the different types of acid sites, pyridine adsorption was used to distinguish the types of acid sites and their relative strength (Figure S3B - F). The characteristic vibrations of pyridine adsorbed on Lewis and Brønsted acid sites were detectable at 1448 and 1540 cm^{-1} , respectively.^{78,79}

According to a previous study, Brønsted acid sites were mostly present in the form of P-OH groups with some contribution from M-OH groups.⁶¹ In contrast, Lewis sites are related to coordinatively unsaturated M^{n+} sites. The ratio between the concentrations of Brønsted and Lewis acid sites on phosphate catalysts is affected by the amount of chemisorbed water. In fact, a Lewis acid site can be converted into a Brønsted site by coordination or dissociative adsorption of water on unsaturated M^{n+} sites.⁶¹

All the catalyst samples possessed both Brønsted and Lewis acidity (Figure S3E and F). LaPO showed the lowest concentration of Brønsted acid sites, but all of them were very strong (Figure S3E and Figure 4). NbPO had the highest concentration of very strong (450 °C) Brønsted acid sites. The distribution of Brønsted acid sites in ZrPO was different; it showed the highest total concentration of Brønsted acid sites of 45 $\mu\text{mol g}^{-1}$ at 150 °C, but only 16 $\mu\text{mol g}^{-1}$ were strong enough to retain pyridine at 450 °C. LaPO has the biggest ionic radius and as a consequence the lowest number of PO_4^{3-} groups in the elementary cell of LaPO_4 . The broad distribution of Brønsted acid site strength showed by ZrPO with respect to the other two samples is in good agreement with the hydrogen

phosphate structure determined by ^{31}P -MAS-NMR. Therefore, the bigger the ionic radius, the smaller is the concentration of Brønsted acid sites in phosphate catalysts.

In contrast, for Lewis acid sites, the three catalysts showed a similar strength distribution (Figure 4 B). NbPO possessed the highest number of Lewis acid sites at every desorption temperature, and there were only few weak Lewis sites. On the contrary, the Lewis acid site concentrations of ZrPO and LaPO were comparable in terms of strong and very strong acid sites, while ZrPO possessed a higher amount of weak and medium strength Lewis acid sites.

The total amount of Brønsted and Lewis acid sites can be ordered as $\text{ZrPO} \approx \text{NbPO} \gg \text{LaPO}$ and $\text{NbPO} > \text{ZrPO} > \text{LaPO}$, respectively. The infrared spectroscopy results showed a decrease in the Lewis acid site concentration trend with increasing ionic character of the M-PO_4 bond ($\text{NbPO} < \text{ZrPO} < \text{LaPO}$). The increase of Lewis acid sites concentration follows an opposite trend with respect to the metal cation size. In fact, the smaller the metal ionic radius, the larger was the number of M-PO_4 unit present in the fundamental unit cell. The distribution of phosphate groups in the unit cell is illustrated in Figure S4.

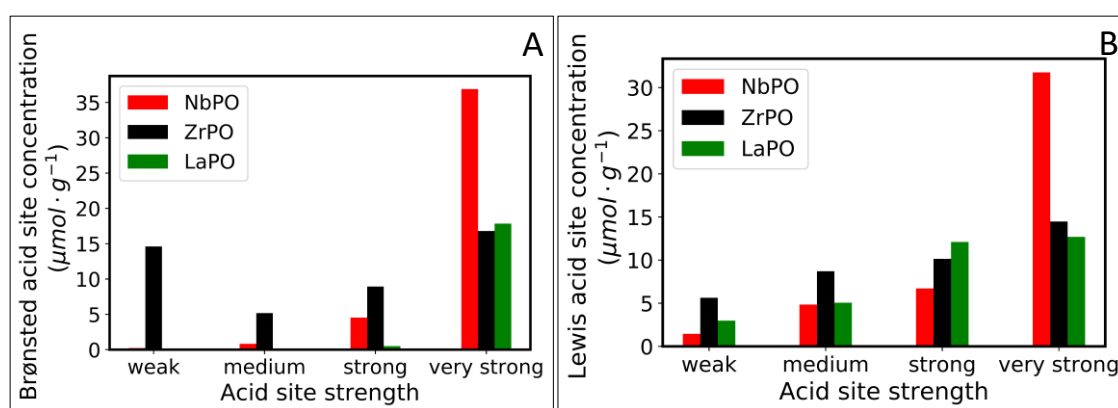


Figure 4. Brønsted (A) and Lewis (B) acid sites concentration and strength distribution. The acid site strength is defined as weak, medium, or strong if pyridine desorbs at temperatures higher than 150, 250, or 350 °C, respectively. Sites that can retain pyridine at 450°C are defined as very strong.

Dihydroxyacetone conversion to lactic acid

Leaching of the metal phosphate was evaluated in a batch reactor containing 0.6 g of catalyst at 90 °C for 4 h. The substrate to catalyst ratio (w/w) was 1.5, and the DHA solution concentration was 0.2 M. XRF analyses of the final reaction solution detected no traces of leached metal, and the amount of phosphorus in solution was negligible (<0.008 mol%).

Assessment of mass transfer limitations

Since mass transfer limitations can affect reaction rates, selectivities, and even the reaction mechanism, it is critical to explicitly assess their relevance for any rigorous kinetic analysis.⁸⁰ Due to the much lower diffusivity of liquids as opposed to gasses, external transport effects are expected to be even more significant when liquid feeds are converted over solid catalysts.⁵⁹

External diffusion limitations were probed by varying the total liquid flow rate and the catalyst mass in the fixed bed by the same factor to provide a constant contact time.

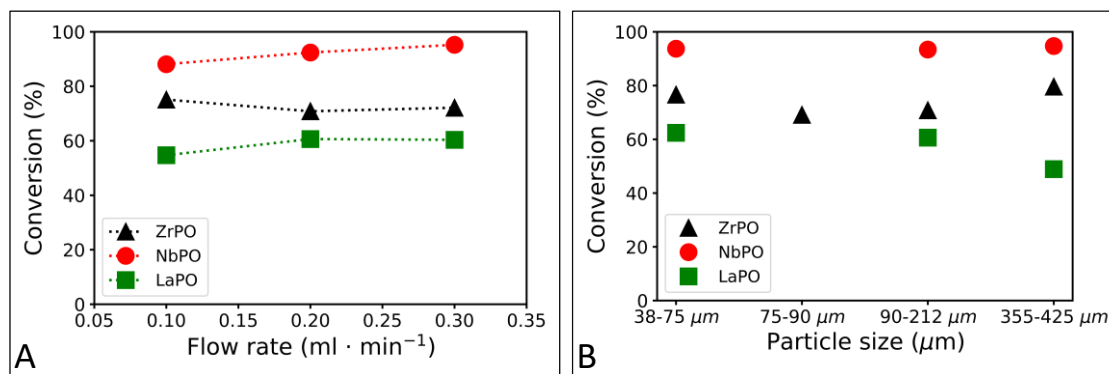


Figure 5. Tests for mass transfer limitations. A: External mass transfer limitations. B: Internal mass transfer limitations. Reaction conditions: 10 bar, 60 g s ml⁻¹, [DHA] = 0.4 M, 150 °C for NbPO and LaPO, 130 °C for ZrPO.

External mass transfer limitations were excluded for ZrPO because the dihydroxyacetone conversion did not increase when the flow rate was raised (Figure 5A). LaPO, although not mass transfer limited under the standard reaction conditions used here (0.2 mL min⁻¹ total flow and 212-90 μm particle size at 150 °C), showed a decline of the DHA conversion when the total flow was decreased to 0.1 mL min⁻¹. In contrast, NbPO is affected by external mass transfer limitation to some extent since DHA conversion steadily increased as the flow rate was raised.

To understand all the significant contributions on the observed rate, the external mass transfer coefficient k_c and the intrinsic rate constant k_s were evaluated for LaPO and NbPO, both assuming a first-order (Table S2) and second-order kinetics (Table 2). The value of k_s was multiplied by the initial concentration of DHA to compare the two constants.

Table 2. Mass transfer coefficient and kinetic constant evaluated at different flow rates for LaPO and NbPO, assuming a second-order kinetic. Reaction conditions: 150 °C, 10 bar, 100 - 300 mg catalyst, [DHA] = 0.4 M. The errors related with k_c and k_s were evaluated by addition of Gaussian noise and iterating the fit.

\dot{V} mL min ⁻¹	v cm min ⁻¹	NbPO				LaPO			
		k_{obs} L mol ⁻¹ s ⁻¹	k_c s ⁻¹	k_s L mol ⁻¹ s ⁻¹	$k_s C_{a0}$ s ⁻¹	k_{obs} L mol ⁻¹ s ⁻¹	k_c s ⁻¹	k_s L mol ⁻¹ s ⁻¹	$k_s C_{a0}$ s ⁻¹
0.1	0.43	0.12	0.0117 ±0.002			0.041	0.04 ±0.04		
0.2	0.85	0.20	0.0234 ±0.004	2±1	0.68	0.053	0.08 ±0.08	0.09 ±0.02	0.04
0.3	1.28	0.31	0.0351 ±0.006			0.053	0.1 ±0.1		

The values reported in Table 2 for the second-order kinetic show that k_c and $k_s C_{a0}$ are the same order of magnitude for LaPO. Thus, neither external mass transfer nor intrinsic kinetics is completely dominant. When raising the flow rate, the value of k_c increased, and its contribution to k_{obs} diminished. In contrast, NbPO k_c is an order of magnitude lower than $k_s C_{a0}$ at all the flows used, meaning that the contribution of external mass transfer to k_{obs} is significant. Moreover, ΔC_A (change of DHA concentration across the boundary layer) is one order of magnitude lower than C_{AB} for NbPO (Figure S5A) and LaPO (Figure S5B), while for ZrPO (Figure S5C) there are three orders of magnitude of difference. These results illustrate that mass transfer limitations are not negligible but also do not exclusively dominate the kinetics under the present conditions. Thus, an explicit deconvolution of k_c and k_s is required for kinetic analysis. Additionally, it is necessary to point out that due to the low apparent density of NbPO, it is not possible to work in a strictly kinetic regime because a further increase in flow rate would cause the catalyst bed to lay outside the isothermal area of the oven (Figure S6). The fluctuation of the value of k_s , with the addition of Gaussian noise to the experimental data for each catalyst, is reported in Figure S7, while the values of k_s and k_c for ZrPO are reported in Table S3.

The internal mass transfer limitations were tested varying the catalyst particle size maintaining the same reaction conditions. NbPO did not suffer from internal mass transfer limitations, while the DHA conversion over LaPO declined when the largest particle size (425-355 μm) was used (Figure 5B). However, LaPO was not limited by internal mass transfer under the standard reaction conditions used here (0.2 mL min⁻¹ total flow and 212-90 μm particle size at 150 °C). Finally, it was possible to exclude the internal mass transfer limitations also for ZrPO since the smallest (75 – 38 μm), and the biggest (425 - 355 μm) particle sizes showed the same conversion (Figure 5B).

Kinetics at different temperatures

All the reactions from 90 to 150 °C reached steady state within 2 h, and no measurable deactivation was seen during a 6 h run (Figure S8). NbPO and ZrPO were the most active catalysts, showing 38 % and 29 % conversion at 90 °C, respectively, while LaPO was almost inactive until 130 °C (Table 3). From 90 °C to 130 °C, the PVA yield over NbPO and ZrPO increased, but it decreased at 150 °C because PVA conversion into LA accelerated. Over LaPO, the PVA yield increased over the whole temperature range, while the LA yield was negligible. On the other hand, ZrPO and NbPO reached 28 % and 42 % LA yield at 150 °C, respectively. The GLA yield was below 1.5 % at every temperature for ZrPO and NbPO, while LaPO showed an increasing GLA yield with temperature. The carbon loss also increased with increasing temperature. A change in the color of the solution was observed as the temperature increased, moving from transparent at 90 °C to an orange-brown color at 150 °C. A similar color change was reported over SnPO, and it was attributed to the formation of

polycondensation products, including humins.²⁵ The pyruvaldehyde and lactic acid yields increased in the following order NbPO > ZrPO > LaPO at each temperature, and these trends are in agreement with the concentrations of Brønsted and Lewis acid sites, respectively. This result was expected since it is well known that Brønsted acid sites are involved in the first dehydration step to produce PVA, while sufficiently strong Lewis acid sites are most effective for the Cannizzaro rearrangements of PVA into LA.⁸¹ LaPO, possessing the metal with biggest ionic radii, is the catalyst with the lowest number of PO₄ groups per unit cell and as a consequence the lowest density of Brønsted acid sites. On the other hand, the total density of Brønsted acid sites was comparable for NbPO and ZrPO, as was their catalytic performances. LaPO started to show reasonable conversion of DHA only at high temperature probably because this catalyst only contained few Brønsted acid sites and the Lewis acid sites, which are less active in dehydration reactions, required a higher temperature to start dehydrating DHA.^{29,82} It is worth noting that the yield of PVA over LaPO was comparable to the yield of undetected carbon at high temperatures. This observation suggest that a high density of Lewis acid sites without a comparable density of Brønsted ones favors side reactions, such as DHA and/or PVA polycondensation.^{45,83}

The apparent activation energies ($E_{a,a}$) for DHA conversion into PVA were 59, 62, and 60 kJ mol⁻¹ for NbPO, ZrPO, and LaPO, respectively (Figure 6A). Fully understanding the mass transfer limitations allowed for the evaluation of the intrinsic kinetic rate constant and the intrinsic activation energy. The intrinsic activation energies ($E_{a,i}$) for NbPO, ZrPO, and LaPO were 71, 62, and 67 kJ mol⁻¹, respectively (Figure 6B). The difference between $E_{a,a}$ and $E_{a,i}$ for NbPO supports the fact that this catalyst is only slightly mass transfer limited. In fact, the apparent activation energy is usually 10 KJ mol⁻¹ or less when a reaction is completely controlled by external mass transfer.⁸⁴

The magnitude of $E_{a,i}$ for the three phosphate catalysts was not very different, suggesting that the catalysts have similar active sites promoting the same kind of chemistry on their surface. Interestingly, the apparent activation energy for LaPO (based on k_{obs}) was the lowest suggesting that the limited conversion over this catalyst was due to an insufficient concentration of Brønsted acid sites. Since strong transport limitations were excluded, this points to the presence of acid sites where the conversion of DHA is sterically hindered. In fact, LaPO is the sole crystalline material in this study.

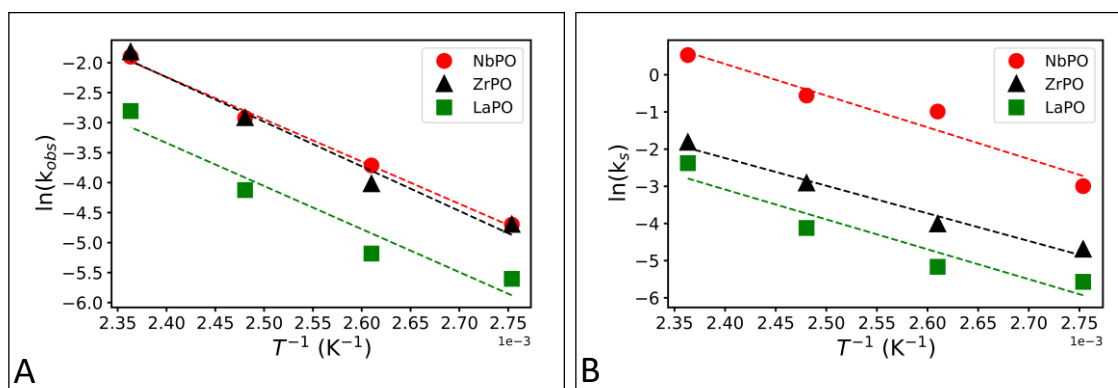


Figure 6. Arrhenius plot for LaPO, NbPO, and ZrPO. A: Based on the observed kinetic rate constant, B: After removing the contribution of the mass transfer limitation from NbPO and LaPO.

Table 3. Catalytic performance of NbPO, ZrPO, and LaPO. Reaction parameters: 200mg catalyst, 0.2 mL min⁻¹ DHA solution flow, [DHA] = 0.4 M, temperature 90÷150 °C, pressure 10 bar, 6h time on stream. DHA = dihydroxyacetone, GLA = glyceraldehyde, PVA = pyruvaldehyde, LA = Lactic Acid, others = pyruvic acid (PA) and glyceric acid (GA), *k* = rate constant, *r_a* = dihydroxyacetone conversion rate. The errors associated with the measurement were calculated based on two repetitions of the same tests if the repetition were three it is indicated by *. If no error is reported it means that the number was obtained by a single catalytic test.

	T °C	X _{DHA} %	Y _{GLA} %	Y _{PVA} %	Y _{LA} %	Y _{others} %	C _{loss} %	k _{obs} ls ⁻¹ mol ⁻¹	r _a mol l ⁻¹ s ⁻¹
NbPO	90	38	1	35	2	2	0	9.2·10 ⁻³	6.0·10 ⁻⁴
	110	61	1	52	5	2	1	2.4·10 ⁻²	6.0·10 ⁻⁴
	130	77	1	55	13	2	6	5.5·10 ⁻²	4.5·10 ⁻⁴
	150	90(±0.6)	1(±0.6)	27(±6)	42(±8)	2(±2)	20(±4)	1.5·10 ⁻²	2.2·10 ⁻⁴
ZrPO	90	29	1	19	3	2	4	9.7·10 ⁻³	7.9·10 ⁻⁴
	110	44(±2)	1(±0.2)	36(±0.6)	5(±1)	1(±1)	1(±0.1)	1.5·10 ⁻²	7.9·10 ⁻⁴
	130	71(±0.3)*	1(±0.3)*	50(±2)*	12(±2)*	3(±1)*	5(±2)*	5.7·10 ⁻²	8.0·10 ⁻⁴
	150	88(±3)	1(±0.3)	44(±2)	28(±0.2)	4(±1)	11(±7)	1.7·10 ⁻²	4.1·10 ⁻⁴
LaPO	90	10(±7)*	0.5(±0.1)*	5(±3)*	2(±1)*	1(±1)*	1(±1)*	3.7·10 ⁻³	4.9·10 ⁻⁴
	110	14(±3)*	1(±0.5)*	9(±2)*	1(±0.5)*	0(±0.5)*	2(±2)*	5.7·10 ⁻³	6.7·10 ⁻⁴
	130	32(±6)*	2(±0.7)*	17(±0.5)*	2(±0.6)*	1(±1)*	9(±4)*	1.6·10 ⁻²	1.2·10 ⁻³
	150	64(±6)*	2(±0.3)*	25(±3)*	4(±1)*	4(±1)*	27(±4)*	6.0·10 ⁻²	1.3·10 ⁻³

Analysis of reaction network

The formation of different products as a function of W/F was analyzed in detail over ZrPO because this catalyst was not affected by transport limitations (Figure 7A). Similar experiments over NbPO and LaPO are shown in the SI (Figure S9). As expected, dihydroxyacetone conversion increased from 20 % to 70 % with increasing contact time, and so did the PVA and lactic acid yields. The carbon loss was lower than 5% at every W/F. "Lost carbon" (C_{loss}) can be formed by decarbonylation of both lactic acid or PVA, and/or the condensation of PVA or DHA to form humins (Figure 1).⁸⁵ To deconvolute the contributions from different side reactions, another set of experiments was performed feeding PVA and LA with varying W/F.

PVA conversion over ZrPO increased with increasing W/F, while glyceraldehyde and dihydroxyacetone yields were negligible at all the W/Fs (Figure 7B). Interestingly, the lactic acid yield increased up to 60 g s ml⁻¹, only to then decrease in favor of C_{loss}. In fact, the yield of lost carbon increased to 4 %, which was in good agreement with the decrease in lactic acid yield. However, it was not possible to completely reject the participation of PVA in the formation of undetected by-products or deposits. Interestingly, at such high W/Fs, the dihydroxyacetone yield slightly increased, suggesting that the interconversion of PVA and DHA approaches an equilibrium at high contact times.

To verify the hypothesized reaction network, reported in Figure 1, a contact time screening was carried out feeding LA over ZrPO. The chromatograms did not show any peaks other than the LA one even when some conversion was observed at high W/Fs (Figure S10). These results support a critical role of LA in the formation of undetected products or deposits (lost carbon), but the reaction solution was transparent. In contrast, when PVA or DHA were used as reactant the product stream was yellowish. Therefore, it is not possible to exclude PVA or DHA contribute to the formation of undetected side products, but it is reasonable to consider their contribution minor compared to that of LA. To gain more insight into the kinetics, the series reaction of DHA to PVA, LA and by-products was modeled with ODEs, S12-S15. The kinetic constants (*k*₁, *k*₂ and *k*₃) at 130 °C for ZrPO were

calculated from the experimental results (feeding DHA, PVA, and LA, respectively) using the equation *S1* and *S11*. Their values, reported in Table S4, were refined through the kinetic modeling. The assumption of a first reaction order for DHA conversion into PVA (Figure S11) was rejected since an apparent second-order reaction better represented the experimental data (Figure 8). The possibility that the apparent second-order behavior is caused by a strong adsorption constant for either PVA or LA was considered. However, we were unable to find a set of chemically-reasonable adsorption constants that describe the data using a first-order kinetic model.

In literature, it is reported that PVA is produced by glyceraldehyde dehydration.²⁷ Some authors hypothesized the possibility to produce PVA directly by dehydrating dihydroxyacetone, which is unlikely based on common reactivity trends in organic chemistry.²⁷ However, none of these possibilities explain an apparent second-order reaction. DHA and GLA are in equilibrium with each other, although DHA seems to be always the most abundant species in solution.⁸⁶ Both are likely to form dimers by protecting the aldehydic or ketonic group.⁸⁶ The possible hemiketal (or hemiacetal) and the dimers formed by the reaction of two dihydroxyacetone molecules or by a combination of dihydroxyacetone and glyceraldehyde are shown in Figure 9. The possible hemiacetals and cyclic intermediate that could be formed from two glyceraldehyde molecules are reported in Figure S14 since they are less likely to be formed while using dihydroxyacetone as reactant. It is reasonable to hypothesize that a hemiketal (Figure 9 a-c-d) or hemiacetal (Figure 9 b) is formed by protecting the C=O moiety of DHA or GLA with an OH of another molecule of DHA or GLA. The hemiketal can successively undergo an intramolecular H-transfer reaction followed by dehydration releasing a molecule of PVA and GLA (or DHA). Additionally, these hemiketal and dimeric intermediate can also promote humins formation. However, it is not possible to exclude glyceraldehyde dehydration as a possible reaction pathway. The complete understanding of the reaction mechanism is beyond the scope of the present work, but a full analysis of the interaction between the catalyst surface and DHA or GLA will be the object of a future dedicated study.

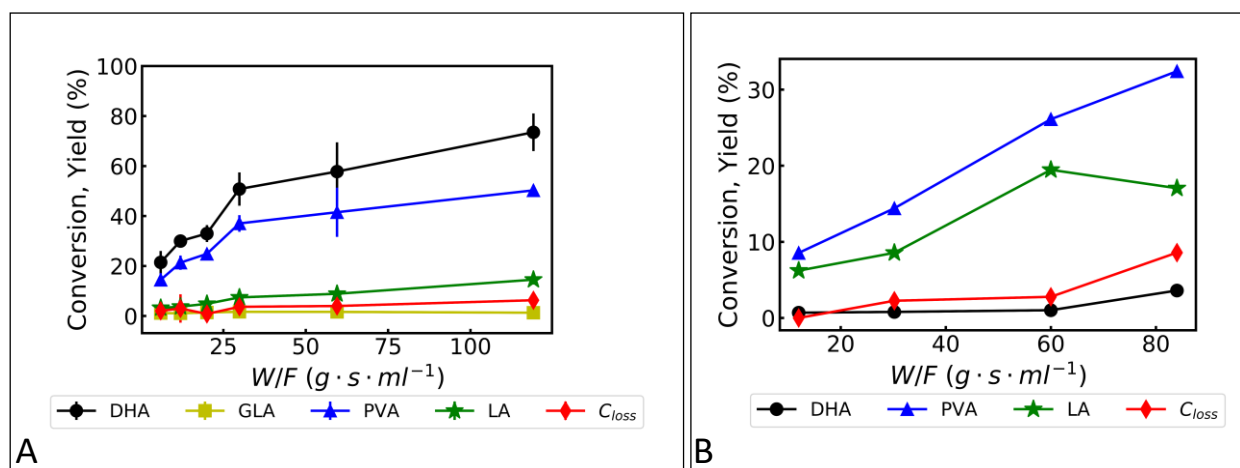


Figure 7. Product distribution over ZrPO as a function of W/F ratio feeding dihydroxyacetone (A) and pyruvaldehyde (B). Reaction conditions: A: 130 °C, 212-90 μ m particle size, 10 bar, [DHA] = 0.4 M. B: 130 °C, 212-90 μ m particle size, 10 bar, [PVA] = 0.4 M.

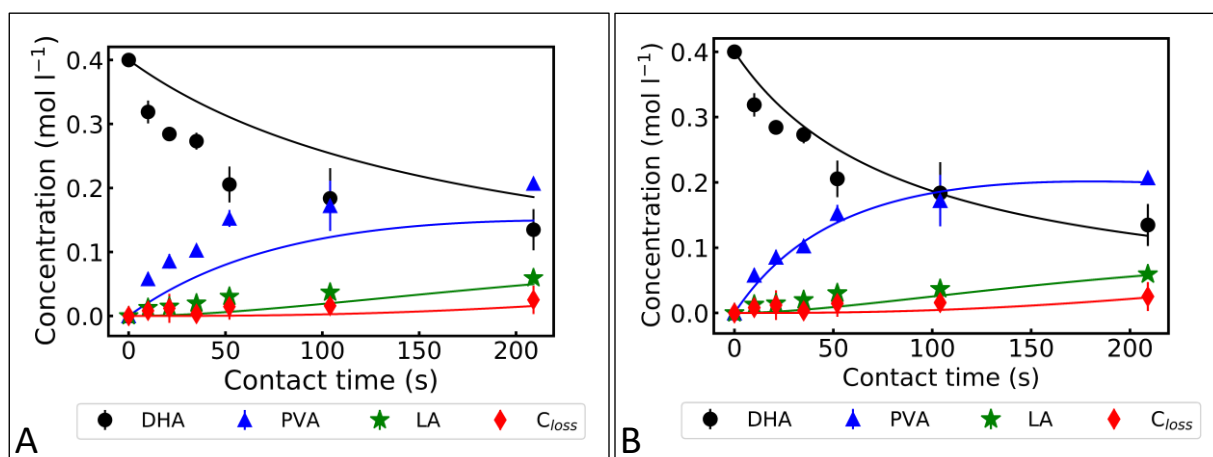


Figure 8. Comparison between the experimental results (reported as dots) and the concentration trends obtained using the kinetic rate constant calculated from the reactivity experiments (left-hand side) and calculated fitting the concentration curve with respect to the experimental points (right-hand side) and assuming a second order reaction for DHA conversion to PVA.

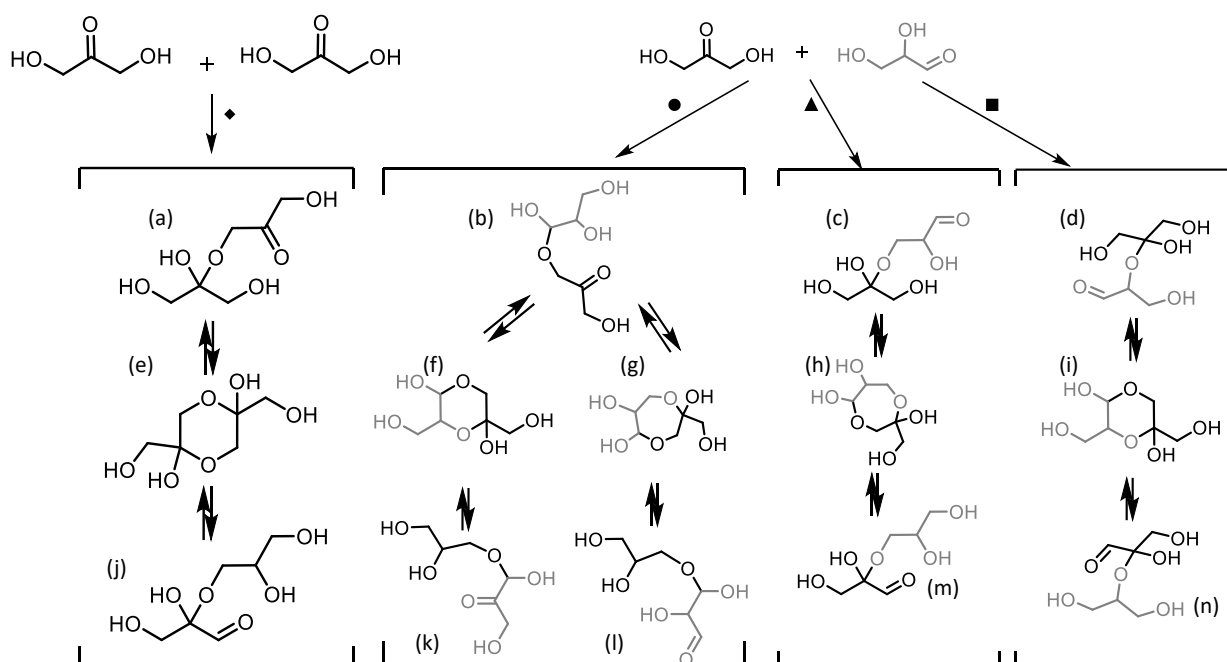


Figure 9. Some of the possible cyclic (e-i) and hemiacetals (a-d and j-n) dimers formed from the reaction of two molecules of DHA (♦) or a molecule of DHA with a GLA one (■▲♦). If the OH-C2 is protecting the C=O bond of DHA (■) the dimer is a six member ring (i) while if the OH-C3 is the protector (▲), the dimer is a seven-member ring (h). In contrast if one of the C-OH of DHA is protecting the C=O of GLA, the final dimer is six or seven-member ring (f or g). The hemiketals/hemiacetals (a-b-c-d) could also form 5-member rings not reported in this figure.

Kinetics of catalyst deactivation

Catalyst deactivation was studied for the two most active catalysts, NbPO and ZrPO. The conversion of DHA over NbPO slowly decreased over time, indicating that the catalyst was deactivating (Figure 10A). The conversion decreased of 2 and 6 percentage points at 150 (from 95 to 92%) and 130 °C (from 68 to 62%), respectively, over 15 h. The overall decrease in conversion, at 150°C, was of 10 percentage points over 30 h (from 95 to 85%). Since analysis of deactivation at high conversion can

be misleading, the evolution of k_1 with respect to time on stream is shown in [Figure S12](#) for both temperatures. The rate constant at 150 °C was constant for 6 h and subsequently decreased over time (the decrease is of 71% at 30 h). In contrast, the rate constant at 130 °C decreased steadily over time to lose 21% of its original value after 15 h on stream. The yield of PVA decreased by 10 percentage points within the first 5 h at 130 °C and it was stable at 40% yield afterwards. In contrast, the yields of the other products were not affected by the deactivation within 15 h (Figure 10B). The product distribution observed at 150 °C (Figure 10A), was more interesting. The LA yield was the highest after 15 h before it started to decrease. The PVA showed the opposite behavior. This observation suggests a selective, slow deactivation of the Lewis acid sites necessary to convert the PVA into LA, whereas the Brønsted acid sites that convert DHA to LA appear to be deactivated to a lesser extent. The amount of lost carbon decreased with decreasing LA yield. This result suggests that undetected carbonaceous species are mainly formed by side reactions of LA, possibly by polymerization. These reactions could likely be reduced by diminishing the initial DHA concentration to have more diluted final LA concentration, but this would increase the costs for subsequent separation steps. Thus, further improvements of the catalyst design appear to be necessary.

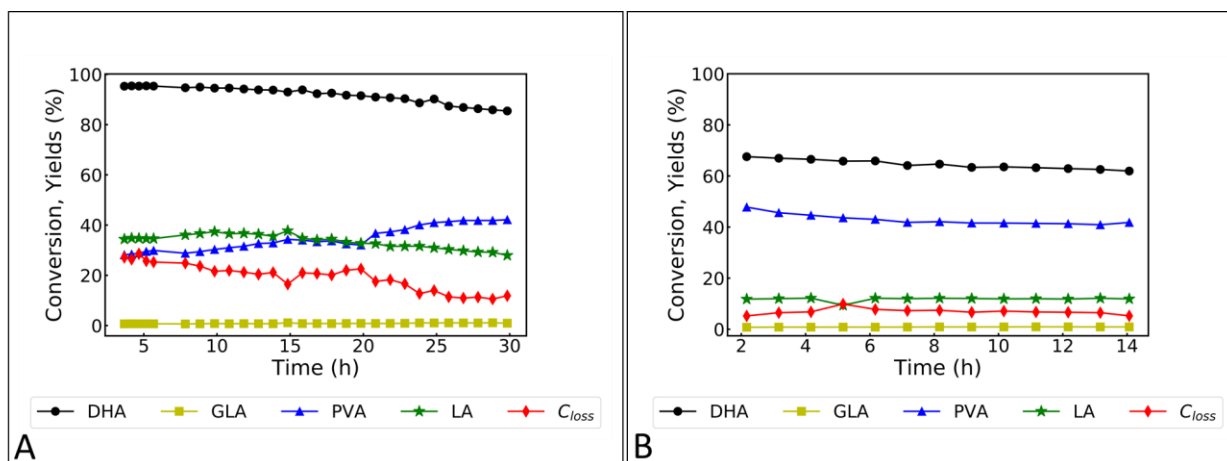


Figure 10. Product distribution over NbPO as a function of time on stream. Reaction conditions: A - 150 °C, 200 mg catalyst, 0.2 mL min⁻¹, 425-355 μ m particle size, 10 bar; B - 130 °C, 200 mg catalyst, 0.2 mL min⁻¹, 90-212 μ m, 10 bar.

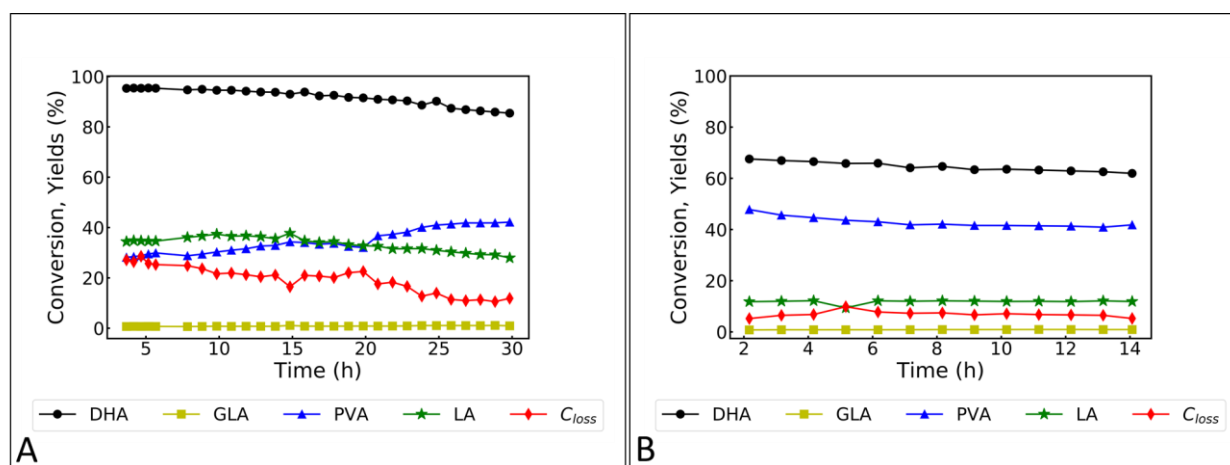


Figure 11. Product distribution over ZrPO as a function of time on stream. Reaction conditions: A - 150 °C, 200 mg catalyst, 0.2 mL min⁻¹, 75-38 μ m particle size, 10 bar; B - 130 °C, 200 mg catalyst, 0.2 mL min⁻¹, 75-38 μ m particle size, 10 bar.

A similar performance was observed for ZrPO (Figure 11B). DHA conversion decreased by only 8 percentage points over 28 h of reaction at 130 °C. The kinetic rate constant steadily decreased for 20 h and reached an apparent steady-state after a 36% reduction (Figure S13B). Interestingly, the conversion was stable around 70% over the first 10 h and around 63% over the last 7 h. The product distribution did not show deactivation over time except for PVA, whose yield decreased by 10% over the first 8 h of reaction. The trend of PVA yield suggests that the concentration of active sites (Brønsted acid sites) is changing over the time. The same deactivation trends were observed at 150 °C (Figure 11A). The kinetic reaction rate constant value steadily diminished over 17 h to reach an apparent steady-state after a 46% reduction (Figure S13A).

Characterization of spent catalyst

NbPO showed the most interesting deactivation and, as a consequence, this catalyst was characterized after reaction. Spent NbPO after 6 and 30 h on stream showed significant weight loss of 10.75% and 24.5% during the temperature programmed oxidation up to 420 °C (Figure S15). The sample after 6 h showed three well defined maxima at 47, 299, and 406 °C, while the sample after 30 h of reaction showed a fourth peak at 123 °C. The high-temperature peaks are related to the decomposition of macromolecules on the catalyst surface, such as poly(lactic acid) and/or humins. In contrast, the lowest temperature can be related to water desorption. The macromolecules can be formed by polycondensation of PVA, DHA, GLA or LA.

The kind of carbon deposited on the catalyst surface after the reaction was characterized by cross-polarized ¹³C-MAS-NMR and ATR-FTIR spectroscopy. The solid-state NMR spectrum (Figure 12) showed 4 peaks in the chemical shift region of aliphatic carbons (12.3, 19.3, 25.5 and 44.2 ppm, sp³ carbon), many convoluted peaks in the aromatic region (148.9, 126.4 and 114.7 ppm, sp² carbon), and three more peaks at 205.5, 173.8 and 84.4 ppm related to ketone, acids or esters, and alcohol or ether moieties, respectively.⁸⁷ The intensity of this spectrum is low because the sample was not isotopically enriched. Despite the low intensity, the spectrum is quite similar to the one reported by Weckhuysen and coworkers for enriched humins derived by alkali or acid treatment of sugars (glucose, fructose, and xylose).^{88,89} The aromatic peaks detected could be related with the presence of either furan- or benzene-derivatives.⁹⁰ Additionally, the intensity in the aromatic region was comparable in intensity to the ketone/aldehyde region, while it was slightly less intense than the aliphatic region. Even though cross-polarization NMR spectroscopy is not quantitative, this suggests that the residual carbon had a diverse chemical makeup. Moreover, the peaks at 173.8 (-C=O), 84.4 (-CH-) and 19.3 ppm (-CH₃) ppm can be tentatively related to poly-lactic acid, whose peaks are at 170, 70 and 17 ppm in its crystalline form.⁹¹ The peak at 84.4 ppm was quite broad, and it can be a convolution of more than one peak, explaining the large shift observed relative to the chemical shift for crystalline lactic acid. This peak was completely absent in the humins spectra reported by Weckhuysen and coworkers.⁸⁸⁻⁹⁰

The infrared spectra of the spent catalysts provided similar results (Figure 13). The very crowded C-H deformation region between 1500 and 1300 cm⁻¹ could be related to the finger-print of the aromatic rings or with the CH, CH₃ deformation vibration of PLA.^{89,92,93} The presence of furans was supported by the peak at 1616 cm⁻¹ related to its C=C.⁹⁰ The quite intense peak at 1709 cm⁻¹ confirmed the presence of C=O as ketonic or aldehydic moieties.⁸⁸⁻⁹⁰ Furthermore, the shoulder at 1749 cm⁻¹ is in strong agreement with the strong C=O of PLA. The shoulder at 1569 cm⁻¹ is assigned to a C=C stretching vibration of an alkene.

Not unexpectedly, the characterization of the carbonaceous deposits showed that the kinetic model involving the loss of carbon through a single first order reaction is simplistic. In fact, the amount of lost carbon and LA acid concentrations are well modeled only at high contact times (at which LA

concentration is high). It is reasonable that at a low concentration of LA, side reactions of PVA or/and DHA are the main contributors to the formation of undetected carbon species. In literature, it is reported that PVA and DHA can produce solid insoluble humins ($\sim 45\%$) and soluble polymers ($\sim 10\%$) by hydrothermal treatment at $220\text{ }^{\circ}\text{C}$.⁸⁵ Additionally, in presence of an acidic catalyst, LA can undergo to dehydration polycondensation.^{94,95} The carbon deposits found on NbPO surface appear to be derived from the polycondensation reaction of DHA, PVA, and LA, which can form the aromatic structures (furanic) by acetal cyclization followed by dehydration.⁸⁵ The deactivation of the active sites responsible for lactic acid formation shown in the left-hand graph of Figure 10 is not surprising. In fact, Lewis acid sites are reported to be active in condensation reactions in the absence of a base.^{83,96,97} Therefore, it is likely that the macromolecules detected by NMR and ATR IR spectroscopy are slowly growing and covering the Lewis acid sites responsible for LA production. This hypothesis explains the decrease in LA yield detected over 30 h and reported in Figure 10.

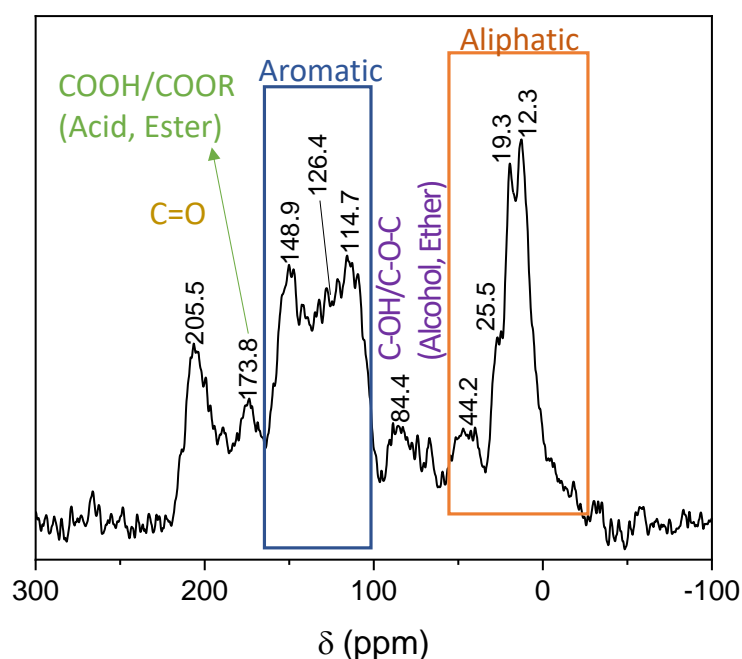


Figure 12. ^{13}C -MAS-NMR spectrum of NbPO after 30 h of reaction.

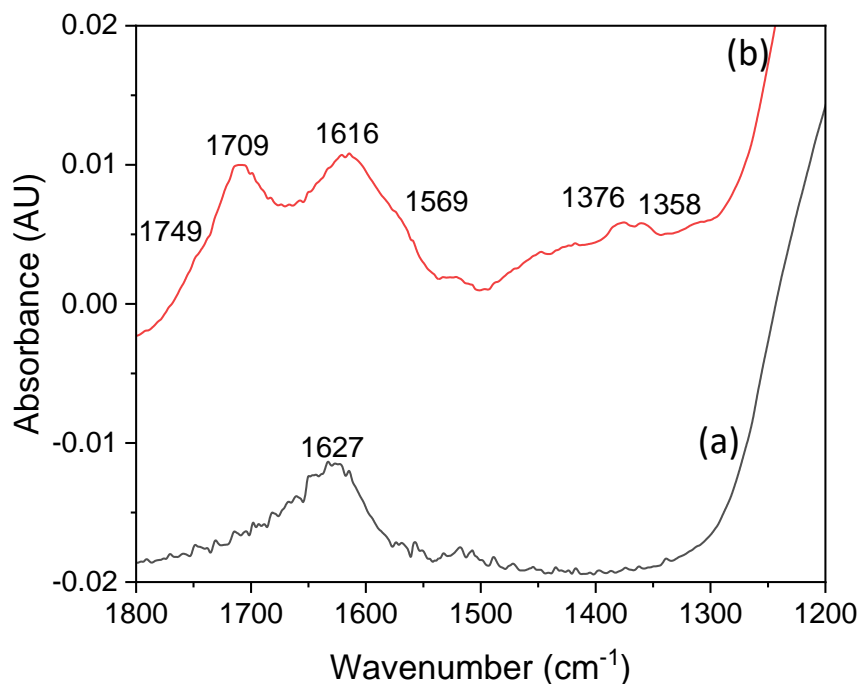


Figure 13. ATR-FTIR spectra of fresh NbPO (a) and NbPO after 30 h of reaction (b).

Conclusions

The continuous aqueous phase conversion of dihydroxyacetone into lactic acid is studied using NbPO, LaPO and ZrPO as catalysts.

NbPO is the most active catalyst, although mass transfer limited, reaching a lactic acid yield of 36 % and 90 % DHA conversion at 150 °C. ZrPO shows a lower LA yield (28 %), while LaPO requires long contact times even to be active towards DHA dehydration. LaPO shows the lowest total concentration of Brønsted acid sites, while NbPO and ZrPO show a concentration of Brønsted acid sites 3 times higher than LaPO. Additionally, LaPO possessed only very strong Lewis acid sites. A combination of strong and very strong Brønsted acid sites seems to better assist the dehydration of DHA. NbPO also shows a higher yield of LA than ZrPO suggesting that very strong Lewis acid sites are required for the Cannizzaro reaction.

The transport limitations for these catalysts are studied in detail. NbPO and LaPO experience external mass transfer limitations to a certain extent, while ZrPO is completely free from mass transfer limitation. Based on experiments at different flow rates, the rate constants of mass transfer and the surface reaction are deconvoluted. An analysis of the reaction products after different contact times shows that DHA is converted to PVA in a second order reaction, indicating a reaction path via a dimeric intermediates.

During a continuous reaction at 150 °C, NbPO slowly deactivates over 30 h of time on stream. The deactivation is more pronounced for Lewis acid sites that are responsible for the conversion of PVA to LA than for Brønsted acid sites that most strongly contribute to DHA conversion to PVA. In fact, the Lewis acid sites are also catalyzing the polycondensation reactions (of LA, PVA or/and DHA), which appear to be responsible for the formation of macromolecules on the catalyst surface. These macromolecules are shown to be similar to humins and polycondensation polymers like PLA.

Acknowledgments

Financial support from the U.S. Nation Science Foundation (grant number: CBET-1705444) is gratefully acknowledged. Qandeel Almas and Michael Stellato are acknowledged for collecting the NH₃-TPD profiles and the ³¹P MAS-NMR spectra, respectively. Ben Comer and Adam Yonge are acknowledged for the help in debugging some of the Python scripts written to produce part of these data and images. Dr. Marco Fraga and Prof. Will Medlin are acknowledged for the fruitful discussions.

References

- (1) Botero, C. D.; Restrepo, D. L.; Cardona, C. A. A Comprehensive Review on the Implementation of the Biorefinery Concept in Biodiesel Production Plants. *Biofuel Res. J.* **2017**, *4* (3), 691–703. <https://doi.org/10.18331/BRJ2017.4.3.6>.
- (2) Lee, R. A.; Lavoie, J.-M. From First- to Third-Generation Biofuels: Challenges of Producing a Commodity from a Biomass of Increasing Complexity. *Anim. Front.* **2013**, *3* (2), 6–11. <https://doi.org/10.2527/af.2013-0010>.
- (3) Ajanovic, A.; Haas, R. On the Future Prospects and Limits of Biofuels in Brazil, the US and EU. *Appl. Energy* **2014**, *135*, 730–737. <https://doi.org/10.1016/j.apenergy.2014.07.001>.
- (4) Bateni, H.; Saraeian, A.; Able, C. A Comprehensive Review on Biodiesel Purification and Upgrading. *Biofuel Res. J.* **2017**, *4* (3), 668–690. <https://doi.org/10.18331/BRJ2017.4.3.5>.
- (5) Katryniok, B.; Kimura, H.; Skrzyńska, E.; Girardon, J.-S.; Fongarland, P.; Capron, M.; Ducoulombier, R.; Mimura, N.; Paul, S.; Dumeignil, F. Selective Catalytic Oxidation of Glycerol: Perspectives for High Value Chemicals. *Green Chem.* **2011**, *13* (8), 1960. <https://doi.org/10.1039/c1gc15320j>.
- (6) Bagnato, G.; Iulianelli, A.; Sanna, A.; Basile, A. Glycerol Production and Transformation: A Critical Review with Particular Emphasis on Glycerol Reforming Reaction for Producing Hydrogen in Conventional and Membrane Reactors. *Membranes (Basel)*. **2017**, *7* (2). <https://doi.org/10.3390/membranes7020017>.
- (7) Razali, N.; Abdullah, A. Z. Production of Lactic Acid from Glycerol via Chemical Conversion Using Solid Catalyst: A Review. *Appl. Catal. A Gen.* **2017**, *543* (April), 234–246. <https://doi.org/10.1016/j.apcata.2017.07.002>.
- (8) Hill, R. G. Biomedical Polymers. *Biomater. Artif. Organs Tissue Eng.* **2005**, 97–106. <https://doi.org/10.1533/9781845690861.2.97>.
- (9) Sinclair, R. G. The Case for Polylactic Acid as a Commodity Packaging Plastic. *J. Macromol. Sci. Part A* **1996**, *33* (5), 585–597. <https://doi.org/10.1080/10601329608010880>.
- (10) Drumright, R. E.; Gruber, P. R.; Henton, D. E. Polylactic Acid Technology. *Adv. Mater.* **2000**, *12* (23), 1841–1846. [https://doi.org/10.1002/1521-4095\(200012\)12:23<1841::AID-ADMA1841>3.0.CO;2-E](https://doi.org/10.1002/1521-4095(200012)12:23<1841::AID-ADMA1841>3.0.CO;2-E).
- (11) Sin, L. T.; Rahmat, A. R.; Rahman, W. A. W. A. Applications of Poly(Lactic Acid). *Handb. Biopolym. Biodegrad. Plast.* **2013**, 55–69. <https://doi.org/10.1016/B978-1-4557-2834-3.00003-3>.
- (12) Castillo Martinez, F. A.; Balciunas, E. M.; Salgado, J. M.; Domínguez González, J. M.; Converti, A.; Oliveira, R. P. de S. Lactic Acid Properties, Applications and Production: A Review. *Trends Food Sci. Technol.* **2013**, *30* (1), 70–83. <https://doi.org/10.1016/j.tifs.2012.11.007>.

- (13) Marketsandmarkets.com. Lactic Acid And Poly Lactic Acid (PLA) Market Analysis By Application (Packaging, Agriculture, Transport, Electronics, Textiles) And Segment Forecasts To 2020. *Marketsandmarkets.Com* **2015**, 1–109. <https://doi.org/978-1-68038-126-9>.
- (14) Mäki-Arvela, P.; Simakova, I. L.; Salmi, T.; Murzin, D. Y. Production of Lactic Acid/Lactates from Biomass and Their Catalytic Transformations to Commodities. *Chem. Rev.* **2014**, *114* (3), 1909–1971. <https://doi.org/10.1021/cr400203v>.
- (15) Hara, M.; Nakajima, K.; Kamata, K. Recent Progress in the Development of Solid Catalysts for Biomass Conversion into High Value-Added Chemicals. *Sci. Technol. Adv. Mater.* **2015**, *16* (3), 1–22. <https://doi.org/10.1088/1468-6996/16/3/034903>.
- (16) Dapsens, P. Y.; Menart, M. J.; Mondelli, C.; Pérez-Ramírez, J. Production of Bio-Derived Ethyl Lactate on GaUSY Zeolites Prepared by Post-Synthetic Galliation. *Green Chem.* **2014**, *16*(2), 589–593. <https://doi.org/10.1039/c3gc40766g>.
- (17) Feliczak-Guzik, A.; Sprynskyy, M.; Nowak, I.; Buszewski, B. Catalytic Isomerization of Dihydroxyacetone to Lactic Acid and Alkyl Lactates over Hierarchical Zeolites Containing Tin. *Catalysts* **2018**, *8* (1), 31. <https://doi.org/10.3390/catal8010031>.
- (18) Lux, S. Catalytic Conversion of Dihydroxyacetone to Lactic Acid with Brønsted Acids and Multivalent Metal Ions. *Chem. Biochem. Eng. Q.* **2016**, *29* (4), 575–585. <https://doi.org/10.15255/CABEQ.2014.2110>.
- (19) Clippel, F. De; Dusselier, M.; Rompaey, R. Van; Vanelderen, P.; Dijkmans, J.; Makshina, E.; Giebler, L.; Baron, G. V.; Denayer, J. F. M.; Pescarmona, P. P.; Jacobs, P. A.; Sels, B. F. Fast and Selective Sugar Conversion to Alkyl Lactate and Lactic Acid with Bifunctional Carbon–Silica Catalysts. *J. Am. Chem. Soc.* **2012**, *134* (24), 10089–10101. <https://doi.org/10.1021/ja301678w>.
- (20) Nakajima, K.; Hirata, J.; Kim, M.; Gupta, N. K.; Murayama, T.; Yoshida, A.; Hiyoshi, N.; Fukuoka, A.; Ueda, W. Facile Formation of Lactic Acid from a Triose Sugar in Water over Niobium Oxide with a Deformed Orthorhombic Phase. *ACS Catal.* **2018**, *8* (1), 283–290. <https://doi.org/10.1021/acscatal.7b03003>.
- (21) Weber, A. L. Prebiotic Sugar Synthesis: Hexose and Hydroxy Acid Synthesis from Glyceraldehyde Catalyzed by Iron(III) Hydroxide Oxide. *J. Mol. Evol.* **1992**, *35* (1), 1–6. <https://doi.org/10.1007/BF00160255>.
- (22) Hayashi, Y.; Sasaki, Y. Tin-Catalyzed Conversion of Trioses to Alkyl Lactates in Alcohol Solution. *Chem. Commun.* **2005**, No. 21, 2716–2718. <https://doi.org/10.1039/b501964h>.
- (23) Jolimaître, E.; Delcroix, D.; Essayem, N.; Pinel, C.; Besson, M. Dihydroxyacetone Conversion into Lactic Acid in an Aqueous Medium in the Presence of Metal Salts: Influence of the Ionic Thermodynamic Equilibrium on the Reaction Performance. *Catal. Sci. Technol.* **2018**, *8*(5), 1349–1356. <https://doi.org/10.1039/c7cy02385e>.
- (24) Rasrendra, C. B.; Fachri, B. A.; Makertihartha, I. G. B. N.; Adisasmito, S.; Heeres, H. J. Catalytic Conversion of Dihydroxyacetone to Lactic Acid Using Metal Salts in Water. *ChemSusChem* **2011**, *4* (6), 768–777. <https://doi.org/10.1002/cssc.201000457>.
- (25) Wang, X.; Liang, F.; Huang, C.; Li, Y.; Chen, B. Highly Active Tin(IV) Phosphate Phase Transfer Catalysts for the Production of Lactic Acid from Triose Sugars. *Catal. Sci. Technol.* **2015**, *5* (9), 4410–4421. <https://doi.org/10.1039/c5cy00647c>.
- (26) Assary, R. S.; Curtiss, L. A. Theoretical Study of 1,2-Hydride Shift Associated with the Isomerization of Glyceraldehyde to Dihydroxy Acetone by Lewis Acid Active Site Models. *J. Phys. Chem. A* **2011**, *115* (31), 8754–8760. <https://doi.org/10.1021/jp204371g>.

- (27) De Clercq, R.; Dusselier, M.; Sels, B. F. Advances in the Conversion of Short-Chain Carbohydrates: A Mechanistic Insight. In *Reaction Pathways and Mechanisms in Thermocatalytic Biomass Conversion I: Cellulose Structure, Depolymerization and Conversion by Heterogeneous Catalysts*; Schlaf, M., Zhang, Z., Eds.; Springer, Singapore, 2016; pp 27–55. https://doi.org/10.1007/978-981-287-688-1_3.
- (28) Ennaert, T.; Van Aelst, J.; Dijkmans, J.; De Clercq, R.; Schutyser, W.; Dusselier, M.; Verboekend, D.; Sels, B. F. Potential and Challenges of Zeolite Chemistry in the Catalytic Conversion of Biomass. *Chem. Soc. Rev.* **2016**, *45* (3), 584–611. <https://doi.org/10.1039/c5cs00859j>.
- (29) Santos, K. M. A.; Albuquerque, E. M.; Innocenti, G.; Borges, L. E. P.; Sievers, C.; Fraga, M. A. The Role of Brønsted and Water-Tolerant Lewis Acid Sites in the Cascade Aqueous-Phase Reaction of Triose to Lactic Acid. *ChemCatChem* **2019**, *11* (13), 3054–3063. <https://doi.org/10.1002/cctc.201900519>.
- (30) Pescarmona, P. P.; Janssen, K. P. F.; Delaet, C.; Stroobants, C.; Houthoofd, K.; Philippaerts, A.; De Jonghe, C.; Paul, J. S.; Jacobs, P. A.; Sels, B. F. Zeolite-Catalysed Conversion of C3 Sugars to Alkyl Lactates. *Green Chem.* **2010**, *12* (6), 1083. <https://doi.org/10.1039/b921284a>.
- (31) Janssen, K. P. F.; Paul, J. S.; Sels, B. F.; Jacobs, P. A. Glyoxylase Biomimics: Zeolite Catalyzed Conversion of Trioses. *Stud. Surf. Sci. Catal.* **2007**, *170* (B), 1222–1227. [https://doi.org/10.1016/S0167-2991\(07\)80981-5](https://doi.org/10.1016/S0167-2991(07)80981-5).
- (32) Dapsens, P. Y.; Mondelli, C.; Pérez-Ramírez, J. Highly Selective Lewis Acid Sites in Desilicated MFI Zeolites for Dihydroxyacetone Isomerization to Lactic Acid. *ChemSusChem* **2013**, *6*(5), 831–839. <https://doi.org/10.1002/cssc.201200703>.
- (33) Dapsens, P. Y.; Kusema, B. T.; Mondelli, C.; Pérez-Ramírez, J. Gallium-Modified Zeolites for the Selective Conversion of Bio-Based Dihydroxyacetone into C1–C4alkyl Lactates. *J. Mol. Catal. A Chem.* **2014**, *388–389*, 141–147. <https://doi.org/10.1016/j.molcata.2013.09.032>.
- (34) Taarning, E.; Saravanamurugan, S.; Holm, M. S.; Xiong, J.; West, R. M.; Christensen, C. H. Zeolite-Catalyzed Isomerization of Triose Sugars. *ChemSusChem* **2009**, *2* (7), 625–627. <https://doi.org/10.1002/cssc.200900099>.
- (35) Yang, X.; Wu, L.; Wang, Z.; Bian, J.; Lu, T.; Zhou, L.; Chen, C.; Xu, J. Conversion of Dihydroxyacetone to Methyl Lactate Catalyzed by Highly Active Hierarchical Sn-USY at Room Temperature. *Catal. Sci. Technol.* **2016**, *6* (6), 1757–1763. <https://doi.org/10.1039/c5cy01037c>.
- (36) Cho, H. J.; Dornath, P.; Fan, W. Synthesis of Hierarchical Sn-MFI as Lewis Acid Catalysts for Isomerization of Cellulosic Sugars. *ACS Catal.* **2014**, *4* (6), 2029–2037. <https://doi.org/10.1021/cs500295u>.
- (37) Feliczak-Guzik, A.; Sprynskyy, M.; Nowak, I.; Jaroniec, M.; Buszewski, B. Application of Novel Hierarchical Niobium-Containing Zeolites for Synthesis of Alkyl Lactate and Lactic Acid. *J. Colloid Interface Sci.* **2018**, *516*, 379–383. <https://doi.org/10.1016/j.jcis.2018.01.090>.
- (38) Feliczak-Guzik, A.; Sprynskyy, M.; Nowak, I.; Buszewski, B. Synthesis and Physicochemical Properties of Hierarchical Zeolites Containing Ruthenium Oxide Nanoparticles and Their Application in the Reaction of Dihydroxyacetone Isomerization. *Microporous Mesoporous Mater.* **2020**, *293*, 109787. <https://doi.org/10.1016/j.micromeso.2019.109787>.
- (39) Takagaki, A.; Goto, H.; Kikuchi, R.; Oyama, S. T. Silica-Supported Chromia-Titania Catalysts for Selective Formation of Lactic Acid from a Triose in Water. *Appl. Catal. A Gen.* **2019**, *570*, 200–208. <https://doi.org/10.1016/j.apcata.2018.11.018>.

- (40) Oberhauser, W.; Evangelisti, C.; Caporali, S.; Dal Santo, V.; Bossola, F.; Vizza, F. Ethyl Lactate from Dihydroxyacetone by a Montmorillonite-Supported Pt(II) Diphosphane Complex. *J. Catal.* **2017**, *350*, 133–140. <https://doi.org/10.1016/j.jcat.2017.04.006>.
- (41) Mylin, A. M.; Levytska, S. I.; Sharanda, M. E.; Brei, V. V. Selective Conversion of Dihydroxyacetone-Ethanol Mixture into Ethyl Lactate over Amphoteric ZrO₂-TiO₂ catalyst. *Catal. Commun.* **2014**, *47*, 36–39. <https://doi.org/10.1016/j.catcom.2014.01.004>.
- (42) Pighin, E.; Díez, V. K.; Di Cosimo, J. I. Synthesis of Ethyl Lactate from Triose Sugars on Sn/Al₂O₃ Catalysts. *Appl. Catal. A Gen.* **2016**, *517*, 151–160. <https://doi.org/10.1016/j.apcata.2016.03.007>.
- (43) Wang, X.; Song, Y.; Huang, L.; Wang, H.; Huang, C.; Li, C. Tin Modified Nb₂O₅ as an Efficient Solid Acid Catalyst for the Catalytic Conversion of Triose Sugars to Lactic Acid. *Catal. Sci. Technol.* **2019**, *9* (7), 1669–1679. <https://doi.org/10.1039/c9cy00257j>.
- (44) Li, L.; Collard, X.; Bertrand, A.; Sels, B. F.; Pescarmona, P. P.; Aprile, C. Extra-Small Porous Sn-Silicate Nanoparticles as Catalysts for the Synthesis of Lactates. *J. Catal.* **2014**, *314*, 56–65. <https://doi.org/10.1016/j.jcat.2014.03.012>.
- (45) Kim, K. D.; Wang, Z.; Jiang, Y.; Hunger, M.; Huang, J. The Cooperative Effect of Lewis and Brønsted Acid Sites on Sn-MCM-41 Catalysts for the Conversion of 1,3-Dihydroxyacetone to Ethyl Lactate. *Green Chem.* **2019**, *21* (12), 3383–3393. <https://doi.org/10.1039/c9gc00820a>.
- (46) Zhang, Z.; ZHAO (Kent), Z. Hydroxyapatite Supported Lewis Acid Catalysts for the Transformation of Trioses in Alcohols. *Chinese J. Catal.* **2011**, *32* (1–2), 70–73. [https://doi.org/10.1016/S1872-2067\(10\)60162-3](https://doi.org/10.1016/S1872-2067(10)60162-3).
- (47) Wang, J.; Masui, Y.; Onaka, M. Conversion of Triose Sugars with Alcohols to Alkyl Lactates Catalyzed by Brønsted Acid Tin Ion-Exchanged Montmorillonite. *Appl. Catal. B Environ.* **2011**, *107* (1–2), 135–139. <https://doi.org/10.1016/j.apcatb.2011.07.006>.
- (48) Wang, X.; Liang, F.; Huang, C.; Li, Y.; Chen, B. Siliceous Tin Phosphates as Effective Bifunctional Catalysts for Selective Conversion of Dihydroxyacetone to Lactic Acid. *Catal. Sci. Technol.* **2016**, *6* (17), 6551–6560. <https://doi.org/10.1039/c6cy00553e>.
- (49) Petrov, I.; Michalev, T. Synthesis of Zeolite A: A Review. *Semant. Sch.* **2012**, No. 51, Book 9.1, 30–35.
- (50) Wang, X.; Song, Y.; Huang, C.; Wang, B. Crystalline Niobium Phosphates with Water-Tolerant and Adjustable Lewis Acid Sites for the Production of Lactic Acid from Triose Sugars. *Sustain. Energy Fuels* **2018**, *2* (7), 1530–1541. <https://doi.org/10.1039/C8SE00140E>.
- (51) Li, X.; Zhixiang, X.; Hongwei, M.; Jinxing, L.; Fukun, L. CN107162892A. CN107162892A, 2017.
- (52) Okuhara, T. Water-Tolerant Solid Acid Catalysts. *Chem. Rev.* **2002**, *102* (10), 3641–3666. <https://doi.org/10.1021/cr0103569>.
- (53) Zhang, Y.; Wang, J.; Ren, J.; Liu, X.; Li, X.; Xia, Y.; Lu, G.; Wang, Y. Mesoporous Niobium Phosphate: An Excellent Solid Acid for the Dehydration of Fructose to 5-Hydroxymethylfurfural in Water. *Catal. Sci. Technol.* **2012**, *2* (12), 2485. <https://doi.org/10.1039/c2cy20204b>.
- (54) Rao, K. T. V.; Souzanchi, S.; Yuan, Z.; Ray, M. B.; Xu, C. (Charles). Simple and Green Route for Preparation of Tin Phosphate Catalysts by Solid-State Grinding for Dehydration of Glucose to 5-Hydroxymethylfurfural (HMF). **2017**, *7* (76), 48501–48511. <https://doi.org/10.1039/C7RA10083C>.
- (55) Saravanan, K.; Park, K. S.; Jeon, S.; Bae, J. W.; Soo Park, K.; Jeon, S.; Wook Bae, J. Aqueous Phase Synthesis of 5-Hydroxymethylfurfural from Glucose over Large Pore Mesoporous

Zirconium Phosphates: Effect of Calcination Temperature. *ACS Omega* **2018**, *3*(1), 808–820. <https://doi.org/10.1021/acsomega.7b01357>.

- (56) Hartman, R. L.; McMullen, J. P.; Jensen, K. F. Deciding Whether to Go with the Flow: Evaluating the Merits of Flow Reactors for Synthesis. *Angew. Chemie - Int. Ed.* **2011**, *50*(33), 7502–7519. <https://doi.org/10.1002/anie.201004637>.
- (57) Tanimu, A.; Jaenicke, S.; Alhooshani, K. Heterogeneous Catalysis in Continuous Flow Microreactors: A Review of Methods and Applications. *Chem. Eng. J.* **2017**, *327*, 792–821. <https://doi.org/https://doi.org/10.1016/j.cej.2017.06.161>.
- (58) Yue, J. Multiphase Flow Processing in Microreactors Combined with Heterogeneous Catalysis for Efficient and Sustainable Chemical Synthesis. *Catal. Today* **2018**, *308*, 3–19. <https://doi.org/https://doi.org/10.1016/j.cattod.2017.09.041>.
- (59) Sievers, C.; Noda, Y.; Qi, L.; Albuquerque, E. M.; Rioux, R. M.; Scott, S. L. Phenomena Affecting Catalytic Reactions at Solid – Liquid Interfaces. *ACS Catal.* **2016**, *6*, 8286–8307. <https://doi.org/10.1021/acscatal.6b02532>.
- (60) West, R. M.; Holm, M. S.; Saravanamurugan, S.; Xiong, J.; Beversdorf, Z.; Taarning, E.; Christensen, C. H. Zeolite H-USY for the Production of Lactic Acid and Methyl Lactate from C3-Sugars. *J. Catal.* **2010**, *269*(1), 122–130. <https://doi.org/10.1016/j.jcat.2009.10.023>.
- (61) Sushkevich, V. L.; Ordonsky, V. V.; Ivanova, I. I. Synthesis of Isoprene from Formaldehyde and Isobutene over Phosphate Catalysts. *Appl. Catal. A Gen.* **2012**, *441–442*, 21–29. <https://doi.org/10.1016/j.apcata.2012.06.034>.
- (62) Kishor Mal, N.; Fujiwara, M. Synthesis of Hexagonal and Cubic Super-Microporous Niobium Phosphates with Anion Exchange Capacity and Catalytic Properties. *Chem. Commun.* **2002**, No. 22, 2702–2703. <https://doi.org/10.1039/B207976C>.
- (63) Kamiya, Y.; Sakata, S.; Yoshinaga, Y.; Ohnishi, R.; Okuhara, T. Zirconium Phosphate with a High Surface Area as a Water-Tolerant Solid Acid. *Catal. Letters* **2004**, *94*(1), 45–47. <https://doi.org/10.1023/B:CATL.0000019329.82828.e4>.
- (64) Malmusi, A. Sustainable Catalytic Processes for the Valorisation of Light Alcohols, Alma Mater Studiorum - Università di Bologna, 2016.
- (65) Brunauer, S.; Emmett, P. H.; Teller, E. Adsorption of Gases in Multimolecular Layers. *J. Am. Chem. Soc.* **1938**, *60*(2), 309–319. <https://doi.org/10.1021/ja01269a023>.
- (66) Barrett, E. P.; Joyner, L. G.; Halenda, P. P. The Determination of Pore Volume and Area Distributions in Porous Substances. I. Computations from Nitrogen Isotherms. *J. Am. Chem. Soc.* **1951**, *73*(1), 373–380. <https://doi.org/10.1021/ja01145a126>.
- (67) Tamura, M.; Shimizu, K. I.; Satsuma, A. Comprehensive IR Study on Acid/Base Properties of Metal Oxides. *Appl. Catal. A Gen.* **2012**, *433–434*, 135–145. <https://doi.org/10.1016/j.apcata.2012.05.008>.
- (68) <http://www.elementalanalysis.com/pixe.html>.
- (69) Jastrzbski, W.; Sitarz, M.; Rokita, M.; Bulat, K. Infrared Spectroscopy of Different Phosphates Structures. *Spectrochim. Acta - Part A Mol. Biomol. Spectrosc.* **2011**, *79*(4), 722–727. <https://doi.org/10.1016/j.saa.2010.08.044>.
- (70) Fang, L.; Shi, Q.; Nguyen, J.; Wu, B.; Wang, Z.; Lo, I. M. C. Removal Mechanisms of Phosphate by Lanthanum Hydroxide Nanorods: Investigations Using EXAFS, ATR-FTIR, DFT, and Surface Complexation Modeling Approaches. *Environ. Sci. Technol.* **2017**, *51*(21), 12377–12384. <https://doi.org/10.1021/acs.est.7b03803>.

- (71) Hezel, A.; Ross, S. D. Forbidden Transitions in the Infra-Red Spectra of Tetrahedral Anions—III. Spectra-Structure Correlations in Perchlorates, Sulphates and Phosphates of the Formula MXO_4 . *Spectrochim. Acta* **1966**, *22* (11), 1949–1961. [https://doi.org/10.1016/0371-1951\(66\)80183-2](https://doi.org/10.1016/0371-1951(66)80183-2).
- (72) Assaaoudi, H.; Ennaciri, A.; Rulmont, A.; Harcharras, M. Gadolinium Orthophosphate Weinschenkite Type and Phase Change in Rare Earth Orthophosphates. *Phase Transitions* **2000**, *72* (1), 1–13. <https://doi.org/10.1080/01411590008224546>.
- (73) Genoveva, G. R.; Enrique, O. R.; Teresita, R. G. E.; Eduardo, O. R. The Influence of Agitation Speed on the Morphology and Size Particle Synthesis of $Zr(HPO_4)_2 \cdot H_2O$ from Mexican Sand. *J. Miner. Mater. Charact. Eng.* **2007**, *06* (01), 39–51. <https://doi.org/10.4236/jmmce.2007.61004>.
- (74) Mudrakovskii, I. L.; Shmachkova, V. P.; Kotsarenko, N. S.; Mastikhin, V. M. ^{31}P Nmr Study of I-IV Group Polycrystalline Phosphates. *J. Phys. Chem. Solids* **1986**, *47* (4), 335–339. [https://doi.org/10.1016/0022-3697\(86\)90022-3](https://doi.org/10.1016/0022-3697(86)90022-3).
- (75) Hudson, M. J.; Workman, A. D.; Adams, R. J. W. High-Resolution Solid-State ^{31}P and ^{15}N Magic-Angle Spinning Nuclear Magnetic Resonance Studies of Amorphous and Microcrystalline Layered Metal(IV) Hydrogenphosphates. *Solid state ionics* **1991**, *46*, 159–165. <https://doi.org/10.1039/JM9910100375>.
- (76) Zah-Letho, J. J.; Verbaere, A.; Jouanneaux, A.; Taulelle, F.; Piffard, Y.; Tournoux, M. “Nb $_2$ -XP $_3$ -YO $_2$,” a Novel NbV Oxophosphate with Disordered Cation Vacancies in a Sc $_2$ (WO $_4$) $_3$ -Type Structure. *J. Solid State Chem.* **1995**, *116* (2), 335–342. <https://doi.org/10.1006/jssc.1995.1223>.
- (77) Girard, G.; Vasconcelos, F.; Montagne, L.; Delevoye, L. ^{31}P MAS NMR Spectroscopy with ^{93}Nb Decoupling and DFT Calculations: A Structural Characterization of Defects in a Niobium-Phosphate Phase. *Solid State Nucl. Magn. Reson.* **2017**, *84*, 210–215. <https://doi.org/10.1016/j.ssnmr.2017.05.003>.
- (78) Zaki, M. I.; Hasan, M. A.; Al-Sagheer, F. A.; Pasupulety, L. In Situ FTIR Spectra of Pyridine Adsorbed on SiO $_2$ –Al $_2$ O $_3$, TiO $_2$, ZrO $_2$ and CeO $_2$: General Considerations for the Identification of Acid Sites on Surfaces of Finely Divided Metal Oxides. *Colloids Surfaces A Physicochem. Eng. Asp.* **2001**, *190* (3), 261–274. [https://doi.org/10.1016/S0927-7757\(01\)00690-2](https://doi.org/10.1016/S0927-7757(01)00690-2).
- (79) G. Busca. The Surface Acidity of Solid Oxides and Its Characterization by IR Spectroscopic Methods . An Attempt at Systematization. *Phys. Chem. Chem. Phys.* **1999**, *1*, 723–736. <https://doi.org/10.1039/A808366E>.
- (80) Davis, M. E., Davis, R. J.; Davis, E. M.; Davis, R. J.; Davis, M. E., Davis, R. J. *Fundamentals of Chemical Reaction Engineering*; 2003; Vol. 43. <https://doi.org/10.1021/ed043pA758.1>.
- (81) Albuquerque, E. M.; Borges, L. E. P.; Fraga, M. A.; Sievers, C. Relationship between Acid–Base Properties and the Activity of ZrO $_2$ -Based Catalysts for the Cannizzaro Reaction of Pyruvaldehyde to Lactic Acid. *ChemCatChem* **2017**, *9* (14), 2675–2683. <https://doi.org/10.1002/cctc.201700305>.
- (82) Nash, C. P.; Ramanathan, A.; Ruddy, D. A.; Behl, M.; Gjersing, E.; Griffin, M.; Zhu, H.; Subramaniam, B.; Schaidle, J. A.; Hensley, J. E. Mixed Alcohol Dehydration over Brønsted and Lewis Acidic Catalysts. *Appl. Catal. A Gen.* **2016**, *510*, 110–124. <https://doi.org/10.1016/j.apcata.2015.11.019>.
- (83) Su, M.; Li, W.; Zhang, T.; Xin, H.; Li, S.; Fan, W.; Ma, L. Production of Liquid Fuel Intermediates from Furfural via Aldol Condensation over Lewis Acid Zeolite Catalysts. *Catal. Sci. Technol.* **2017**, *7* (16), 3555–3561. <https://doi.org/10.1039/C7CY01028A>.

- (84) Fogler, H. S. Diffusion and Reactions. In *Elements of Chemical Engineering*; Pearson Education Inc., 2006; pp 813–866.
- (85) Shi, N.; Liu, Q.; Ju, R.; He, X.; Zhang, Y.; Tang, S.; Ma, L. Condensation of α -Carbonyl Aldehydes Leads to the Formation of Solid Humins during the Hydrothermal Degradation of Carbohydrates. *ACS Omega* **2019**, *4* (4), 7330–7343. <https://doi.org/10.1021/acsomega.9b00508>.
- (86) A. Yaylayan, V.; Harty-Majors, S.; A. Ismail, A. Investigation of DL-Glyceraldehyde-Dihydroxyacetone Interconversion by FTIR Spectroscopy. *Carbohydr. Res.* **1999**, *318*(1–4), 20–25. [https://doi.org/10.1016/S0008-6215\(99\)00077-4](https://doi.org/10.1016/S0008-6215(99)00077-4).
- (87) Clayden, J.; Greeves, N.; Warren, S. G.; Wothers, P. *Organic Chemistry*, 2nd ed.; Oxford University Press: Oxford, 2001.
- (88) van Zandvoort, I.; Koers, E. J.; Weingarh, M.; Bruijninx, P. C. A.; Baldus, M.; Weckhuysen, B. M. Structural Characterization of ^{13}C -Enriched Humins and Alkali-Treated ^{13}C Humins by 2D Solid-State NMR. *Green Chem.* **2015**, *17* (8), 4383–4392. <https://doi.org/10.1039/C5GC00327J>.
- (89) van Zandvoort, I.; Wang, Y.; Rasrendra, C. B.; van Eck, E. R. H.; Bruijninx, P. C. A.; Heeres, H. J.; Weckhuysen, B. M. Formation, Molecular Structure, and Morphology of Humins in Biomass Conversion: Influence of Feedstock and Processing Conditions. *ChemSusChem* **2013**, *6* (9), 1745–1758. <https://doi.org/10.1002/cssc.201300332>.
- (90) van Zandvoort, I.; R. H. van Eck, E.; de Peinder, P.; J. Heeres, H.; C. A. Bruijninx, P.; M. Weckhuysen, B. Full, Reactive Solubilization of Humin Byproducts by Alkaline Treatment and Characterization of the Alkali-Treated Humins Formed. *ACS Sustain. Chem. & Eng.* **2015**, *3* (3), 533–543. <https://doi.org/10.1021/sc500772w>.
- (91) A. M. Thakur, K.; T. Kean, R.; M. Zupfer, J.; U. Buehler, N.; A. Doscotch, M.; J. Munson, E. Solid State ^{13}C CP-MAS NMR Studies of the Crystallinity and Morphology of Poly(L-Lactide). *Macromolecules* **1997**, *29* (27), 8844–8851. <https://doi.org/10.1021/ma960828z>.
- (92) Tai, H.; Upton, C. E.; White, L. J.; Pini, R.; Storti, G.; Mazzotti, M.; Shakesheff, K. M.; Howdle, S. M. Studies on the Interactions of CO_2 with Biodegradable Poly(DL-Lactic Acid) and Poly(Lactic Acid-Co-Glycolic Acid) Copolymers Using High Pressure ATR-IR and High Pressure Rheology. *Polymer (Guildf.)* **2010**, *51* (6), 1425–1431. <https://doi.org/10.1016/j.polymer.2010.01.065>.
- (93) Kang, S.; Hsu, S. L.; Stidham, H. D.; Smith, P. B.; Leugers, M. A.; Yang, X.; Ling Hsu, S.; D. Stidham, H.; B. Smith, P.; Anne Leugers, M.; Yang, X. A Spectroscopic Analysis of Poly(Lactic Acid) Structure. *Macromolecules* **2001**, *34* (13), 4542–4548. <https://doi.org/10.1021/ma0016026>.
- (94) Takasu, A.; Narukawa, Y.; Hirabayashi, T. Direct Dehydration Polycondensation of Lactic Acid Catalyzed by Water-Stable Lewis Acids. *J. Polym. Sci. Part A Polym. Chem.* **2006**, *44* (18), 5247–5253. <https://doi.org/10.1002/pola.21639>.
- (95) Mehta, R.; Kumar, V.; Bhunia, H.; Upadhyay, S. N. Synthesis of Poly(Lactic Acid): A Review. *J. Macromol. Sci. Part C Polym. Rev.* **2005**, *45* (4), 325–349. <https://doi.org/10.1080/15321790500304148>.
- (96) Mahrwald, R. Diastereoselection in Lewis-Acid-Mediated Aldol Additions. *Chem. Rev.* **1999**, *99* (5), 1095–1120. <https://doi.org/10.1021/cr980415r>.
- (97) Hassan, Y.; Klein, R.; Kaye, P. T. Aldol Condensation Reactions Effectively Catalysed by Lewis Acid. *Acta Chem. IASI* **2017**, *25* (1), 63–72. <https://doi.org/10.1515/achi-2017-0007>.

